Quantifying the effects of cell death and agar density on yeast colony biofilms using an extensional flow mathematical model

Alexander K. Y. Tam[1,*], Daniel J. Netherwood[2], Jennifer M. Gardner[3], Jin Zhang[3], Campbell W. Gourlay[4], Vladimir Jiranek[5], Benjamin J. Binder[2], and J. Edward F. Green[2]

[1]UniSA STEM, The University of South Australia, Mawson Lakes SA 5095, Australia

[2]School of Computer and Mathematical Sciences, The University of Adelaide, Adelaide SA 5005, Australia

[3]Department of Wine Science, School of Agriculture, Food and Wine, The University of Adelaide, Glen Osmond SA 5064, Australia

[4]Kent Fungal Group, School of Biosciences, The University of Kent, Canterbury, Kent, United Kingdom

[5]School of Biological Sciences, The University of Southampton, Southampton, United Kingdom

*Correspondence: alex.tam@unisa.edu.au

Abstract: We used a combination of experiments, mathematical modelling, and parameter estimation to better understand how agar density affects colony biofilm growth of the yeast species *Saccharomyces cerevisiae*. We obtained 15 total experimental replicates on rectangular plates filled with 0.6%, 0.8%, 1.2%, and 2.0% agar. In the experiments, we measured the horizontal expansion over time, the proportion of living cells, and the colony biofilm aspect ratio, to quantify the colony biofilm size, composition, and shape, respectively. We modelled colony biofilm expansion using a thin-film extensional flow mathematical model. Fitting five unknown model parameters to mean experimental data revealed that nutrient uptake decreases and biofilm–substratum adhesion strength increases on harder agar. Sensitivity analysis, fitting to individual replicates, and synthetic data analysis confirmed that increased biofilm–substratum adhesion is the most consistent effect of harder agar. This finding aligns with similar results reported for bacteria, and suggests that substratum mechanics are important for yeast colony biofilm growth.

Keywords: Lubrication theory, thin-film approximation, viscous flow, multiphase flow, slip, *Saccharomyces cerevisiae*, parameter estimation

---

1 Introduction and Background

Biofilms are surface-dwelling communities of cells embedded within a viscous extracellular matrix (ECM) composed of extracellular polymeric substances (EPS) [1–3]. The bakers' yeast *Saccharomyces cerevisiae* is an important model organism in cell biology [4, 5], because of its ease of use in experiments and its similarity to higher eukaryotic cells [6]. Reynolds and Fink [7] developed an assay for *S. cerevisiae* biofilm formation, which requires the Flo11p glycoprotein known to promote cell-to-surface adhesion. Grown on agar media, the yeast forms a confluent mat that can fill a 90 mm Petri dish in under two weeks [8–10]. These single-species mats are less complex than naturally-occurring biofilms, but still involve the key feature of extracellular matrix deposition. Throughout this work, we use the term *colony biofilm* to refer to a single-species mat. Due to similarities between yeast and the bacterium *Mycobacterium smegmatis* [11], Reynolds and Fink [7] hypothesised that the yeast colony biofilm expands by sliding motility. This term refers to passive growth [12] where the cells and fluid expand as a unit, with low surface tension and weak adhesion to the substratum. Mathematical modelling, when combined with experimental observations, enables us to better understand these mechanisms of growth.

Mathematical modelling of colony biofilm growth is an established field [13, 14], encompassing agent-based [15–19], reaction–diffusion [20–28], and continuum mechanical [29–43] approaches. The earliest and most common colony biofilm models consider growth in a liquid culture medium from which it obtains nutrients [44, 45]. In contrast, mat formation experiments involve a yeast colony biofilm spreading over an agar medium, bounded above by air. This scenario has been addressed previously by several authors [34–36, 46–50]. For *S. cerevisiae* specifically, a thin-film extensional flow mathematical model effectively characterises colony biofilm expansion by sliding motility [36]. However, Tam et al. [36] neglected cell death when comparing the model with experiments. In harsh environments, yeast cells will die by accidental cell death [51, 52], but can also undergo regulated cell death [22, 53] which releases nutrient for the benefit of the colony. Another limitation is that Tam et al. [36] only considered experiments on soft, low-density (0.3%) agar. Recent work [54, 55] has also explored how agar density and cell–substratum adhesion impact growth in bacterial colonies [29, 54–56]. These works have revealed that hard, high-density substrates tend to reduce nutrient uptake [56], increase cell–substrate friction [55], promote wrinkle formation [29], and favour vertical over horizontal growth, increasing the biofilm–agar contact angle [55]. However, although we expect these effects of varying agar density to occur in *S. cerevisiae* colonies as well, their prevalence and underlying mechanisms remain largely unexplored in fungal colonies.

We combine experiments and mathematical modelling to quantify cell death and agar density in *S. cerevisiae* yeast colony biofilms. In Section 2 we describe our rectangular experimental assay and the image processing procedure. These yield a total of 15 experimental colony biofilms on 0.6%, 0.8%, 1.2%, and 2.0% agar. We obtain measurements for colony biofilm width over time, cell viability data at three spatial locations, and a measure of the aspect ratio. Like bacteria [55], in our experiments harder agar favours vertical growth over horizontal growth. To interpret these new experimental results, we modify the thin-film extensional flow model of Tam et al. [36] to incorporate colony biofilm composition data and the impact of cell–substrate adhesion. We then perform a more detailed comparison with experiments than our previous work. Using numerical optimisation, we fit five unknown parameters to the experimental data, obtaining a set of optimal parameters for each agar density. Consistent with previous studies in bacteria [55, 56], increased agar density reduces nutrient uptake and increases cell–substratum friction. In contrast, biomass production rate, cell death rate, and nutrient consumption rate have less variability across agar densities. We confirm the robustness of these results using parameter sensitivity analysis and synthetic simulations. These analyses suggest that differences in cell–substratum adhesion are robust, whereas differences in nutrient uptake are less robust. Thus, we confirm that cell–substratum adhesion is a vital mechanism explaining differentiated growth of *S. cerevisiae* colony biofilms on varying density media.

2 Yeast Colony Biofilm Experiments

A total of 15 experimental yeast colonies were grown in rectangular Petri dishes, across agar densities $a \in \{0.6, 0.8, 1, 2, 2.0\}\%$. All replicates were stained using Phloxine B dye ($10\,\mu\text{M}$), to indicate locations of cell death [57, 58]. For each replicate, we took eight photographs on Days $2, 4, 6, 8, 10, 12, 14$, and 21, and used image processing to obtain the colony biofilm width. We also measured the proportions of living and dead cells in the colony biofilm, averaged over one replicate on 0.6% and one replicate on 2.0% agar, on Day 14 of the experiments. Total cell counts were obtained on Day 21, which we used to estimate the aspect ratio. We introduce the following notation for experimental measurements, enabling comparison with the mathematical model:

- $S_i(t_j; a)$: Experimental colony biofilm half-width for replicate $i = 1, 2, 3, 4$ on agar density a, at time t_j, for $j = 1, \ldots, 8$, where t_j represents the time of the j-th photograph.
- $\Phi_k = \Phi(x_k)$: Cell volume fraction at spatial position x_k, for $k = 1, 2, 3$, averaged over all replicates and agar densities. The three measurements were taken at approximately $x_1 = 0$, $x_2 = S(t)/2$,

and $x_3 = S(t)$, where $t = 14$ days.

- $A(a)$: Colony biofilm aspect ratio on agar density a, averaged over all replicates. The aspect ratio is defined as the colony biofilm's maximum vertical thickness divided by its mean half-width. We obtained one estimate per experiment, on Day 21.

When comparing the model with experiments, we ensure that quantities are dimensionless by scaling the experimental results according to the model nondimensionalisation introduced in Section 3.

2.1 Experimental Method

Σ1278b, a diploid prototrophic strain of *Saccharomyces cerevisiae*, was used in these experiments. Yeast Peptone Dextrose (YPD) medium ($10\,\mathrm{g\,L^{-1}}$ yeast extract, $20\,\mathrm{g\,L^{-1}}$ peptone, $20\,\mathrm{g\,L^{-1}}$ glucose) either as a liquid or with 0.6, 0.8, 1.2 and 2.0% agar for solid media was prepared by filter sterilising 2 × YPD and mixing with an equal volume of molten 12, 16, 24 or $40\,\mathrm{g\,L^{-1}}$ (BD Bacto™ Agar, Becton, Dickinson and Company, New Jersey, USA). Phloxine B was also added to YPD agar at 10 µM. A 5 mL yeast culture was grown for 24 hours in liquid YPD prior to inoculation on plates. A straight streak of yeast culture was applied to YPD agar in a 100 mm square Petri dish with a 4.5 mm plastic inoculation loop guided along a suspended ruler edge. The initial cell density was $1.2 \times 10^8\,\mathrm{cells\,mL^{-1}}$ and the streak width approximately 2 mm. Plates were cling wrapped and incubated agar side down for up to 21 days at 25 °C. Macroscopic plate images were captured with an Apple iPhone 12 Pro. Cross sections that spanned the entire width of the colony biofilm streak (and 5 mm tall) were cut from plates with a scalpel and imaged using a Nikon Eclipse 50i microscope and Nikon camera (DS-2MBW, Nikon, Japan). Multiple images were taken across each section and stitched together with Fiji software (ImageJ).

The proportion of stained cells from samples from plates was measured by flow cytometry with a Guava 12 HT system and Guava EasyCyte™ software (Luminex, Yokohama, Japan; formerly Millipore, Darmstadt, Germany). The flow cytometry was equipped with Violet (405 nm), Blue (488 nm, 150 mW), Red (642 nm) excitation lasers, along with 450/45 nm and 664/20 nm emission filters. Cell samples were collected with sterile pipette tips or washed from 2 or $4\,\mathrm{cm^2}$ agar slices spanning the entire width of the area containing yeast and diluted in 5 mL phosphate buffered saline. Cells fluorescent due to the uptake of Phloxine B were considered non-viable. In parallel, the total number of cells was also enumerated using a hemocytometer and a Nikon Eclipse 50i microscope.

2.2 Image Processing and Quantification

We obtained a time series of photographs of the yeast colony biofilm for each experimental replicate. Example photographs from one replicate on 0.6% agar and one replicate on 2.0% agar are shown in Figure 2.1. To obtain the colony biofilm width in an experimental photograph, we used the known

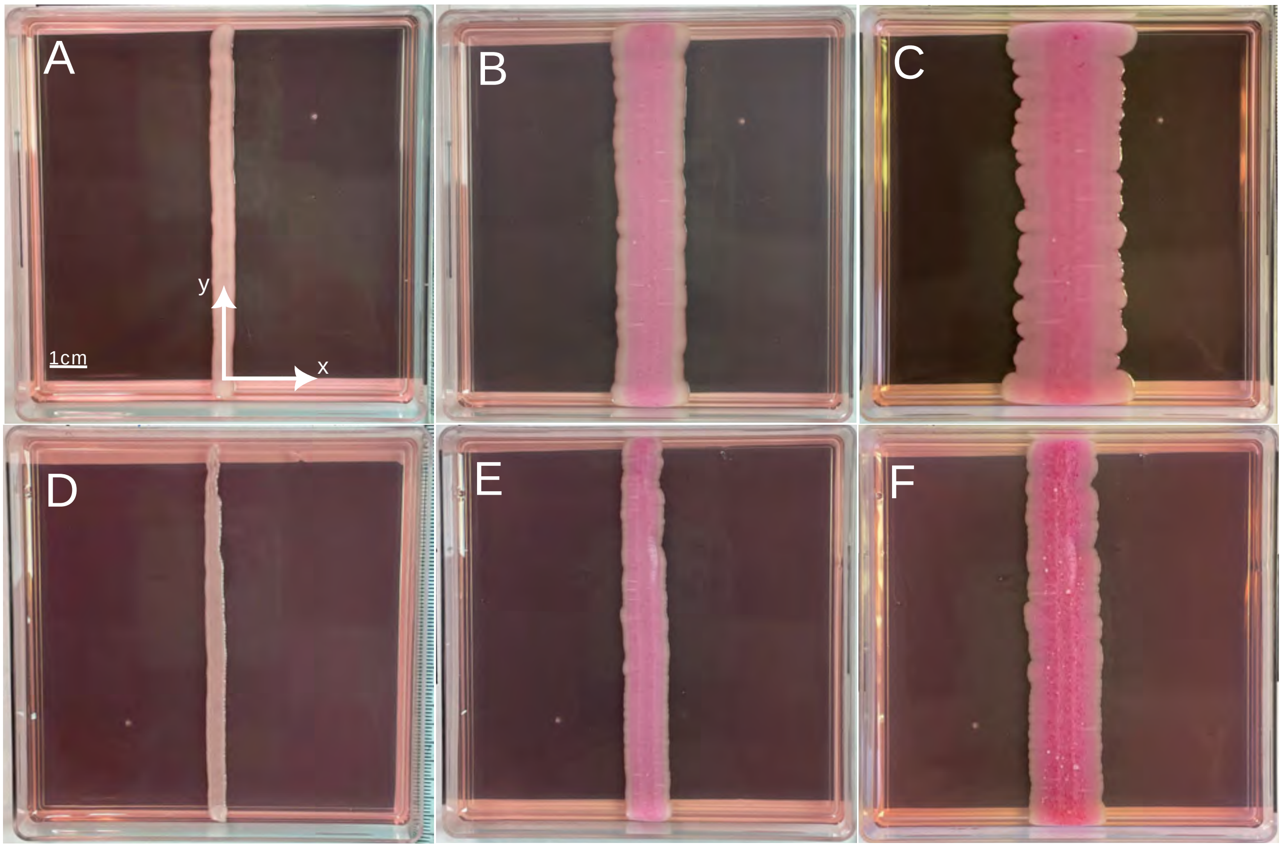

Figure 2.1: Experimental photographs of yeast colony biofilm growth over 21 days on 0.6% and 2.0% agar. Darker pink indicates regions of dead cells stained with Phloxine B. (A) Colony biofilm grown on 0.6% agar (Day 2), with axes and scale bar included. (B) Colony biofilm grown on 0.6% agar (Day 10). (C) Colony biofilm grown on 0.6% agar (Day 21). (D) Colony biofilm grown on 2.0% agar (Day 2). (E) Colony biofilm grown on 2.0% agar (Day 10). (F) Colony biofilm grown on 2.0% agar (Day 21).

Petri dish size of 100 mm to determine the physical distance corresponding to a pixel. After obtaining this scaling factor, we manually rotated and cropped each photograph to remove the Petri dish from the image. We then used JULIA's `FileIO` package and `Images` library to import the photograph and apply Otsu's method to obtain a binary image. We then computed the total number of visible pixels in the colony biofilm, divided by the number of pixels in the y-direction of the photograph, and applied the scaling factor, to determine an approximation for the colony biofilm width. The mean colony biofilm half-widths over time for all agar densities are shown in Figure 2.2.

Our experiments also provide measurements of the proportions of living and dead cells. Photographs

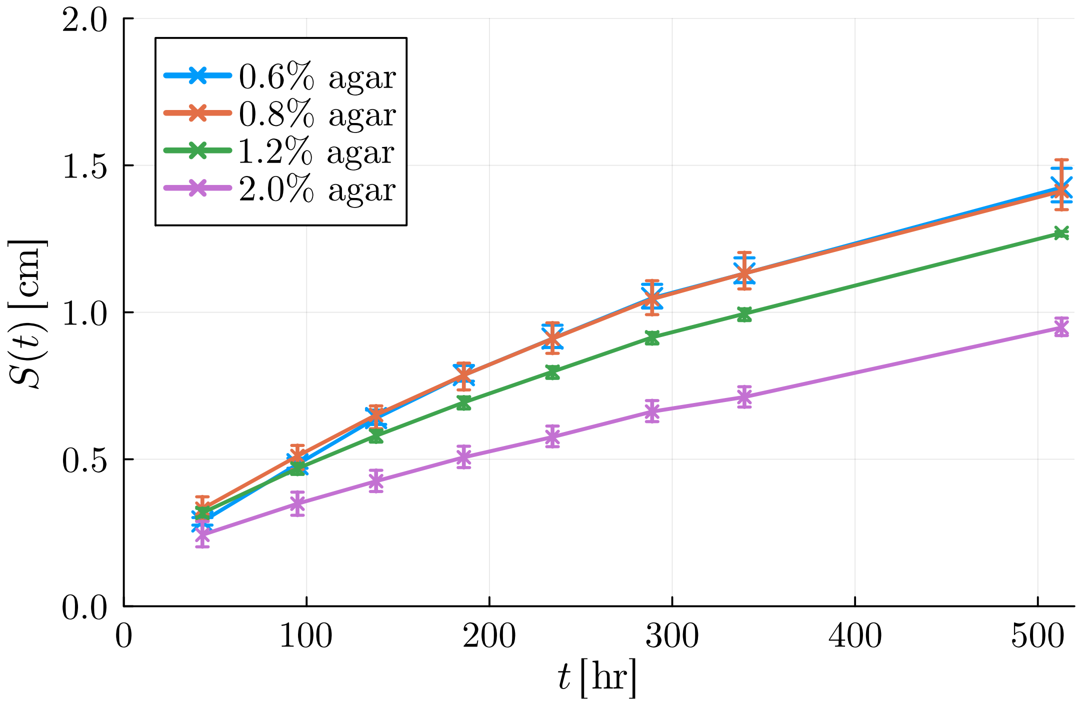

Figure 2.2: Mean experimental half-width, $S(t)$ for colony biofilms grown on different density agar media, plotted against time. Error bars indicate the range observed across all experiments ($n = 4$ for all agar densities, except $n = 3$ for 2.0% agar).

of colonies stained with Phloxine B (Figure 2.1) suggest that the proportion of living cells is maximum at the leading edge, and decreases towards the centre of the colony biofilm. To investigate overall cell viability, we obtained one measurement from a colony biofilm on soft (0.6%) agar, and one measurement from a colony biofilm on hard (2.0%) agar. Both measurements were taken on Day 14. In sampling from a $2\,\mathrm{cm}^2$ region of agar across the full width of the colony biofilm, we found 89.5% total cell viability on soft (0.6%) agar, and 89.9% on hard (2.0%) agar. Since there was negligible difference in overall viability between agar densities, we assumed that each colony biofilm has the same composition regardless of replicate and agar density. We then obtained smaller samples from the same two colonies at three localised regions of the colony biofilm, to quantify how cell viability depended on position. Averaging across both 0.6% and 2.0% agar, we obtained the results shown in Table 2.1. In previous experiments, some colony biofilms stained with Phloxine B included a red ring of elevated cell death near the rim, which could be due to regulated cell death [22]. However, we did not observe an analogous region in these experiments. Instead, the proportion of dead cells is highest in the centre of the colony biofilm, and decreases towards the leading edge (Table 2.1). This observation suggests that cell death is predominantly due to accidental cell death in these colony biofilms, as reported by Netherwood et al. [22].

Table 2.1: Average colony biofilm composition (proportion of living cells) at three regions along the colony biofilm. Proportions averaged from one replicate each on 0.6% and 2.0% agar, on Day 14.

Centre ($x_1 = 0$)	**Middle** ($x_2 = S(t)/2$)	**Edge** ($x_3 = S(t)$)
0.855	0.874	0.918

We used cross-sectional microscopy and cell count data to estimate the colony biofilm thickness. One limitation of our experimental method is that measuring the vertical profile was only possible after cutting the colony biofilm and imaging the cross-section. During cutting, the biofilm–substratum and biofilm–air interfaces of colonies grown on soft agar changed shape significantly. Consequently, we could not obtain reliable thickness measurements for colony biofilms grown on soft agar. Given these experimental challenges, we only measured the physical aspect ratio from micrographs of colony biofilm cross-sections on hard (2.0%) agar, such as Figure 2.3. This yielded the aspect ratio of $A(2.0) = 0.0683$ for 2.0% agar.

Figure 2.3: Cross-section of a colony biofilm grown on 2.0% agar, after 21 days of growth. We used this micrograph to measure the physical aspect ratio for 2.0% agar. We subsequently estimated the aspect ratio for 0.6%, 0.8%, and 1.2% agar using cell count data.

We used total cell counts to estimate the aspect ratios for 0.6%, 0.8%, and 1.2% agar. Cell count data were collected using a hemocytometer and a Nikon Eclipse 50i microscope on Day 21, providing an accurate measure of biomass volume. For each experiment, we used a 1 cm strip to count the mean number of cells per mm in the y-direction of the dish. The ratio of cell count to mean width then provided an estimate for the colony biofilm thickness, in cells per unit area in the (x, y) plane. Provided the cell sizes and colony biofilm compositions are similar for each agar density, the ratio of thickness in cells mm^{-2} to half-width in mm will be approximately proportional to the physical aspect ratio. Consequently, we estimated the physical aspect ratio by scaling the cell count aspect ratio, by a factor chosen to ensure that the aspect ratio for 2.0% agar is the measured value, $A(2.0) = 0.0683$. Table 2.2 shows these calculations, and the quantitative trends are consistent with the observations that colonies are thicker on harder agar than on softer agar.

Table 2.2: Aspect ratio calculations based on the experimental cell count data from Day 21 on agar media of different density.

Agar Density, a (%)	n	**Mean Count** ($\text{cells}\,\text{mm}^{-1}$)	**Mean Half-Width** (mm)	**Mean Thickness** ($\text{cells}\,\text{mm}^{-2}$)	**Aspect Ratio,** $A(a)$
0.6	4	1.06×10^8	14.3	7.44×10^7	0.0306
0.8	4	1.40×10^8	14.1	9.91×10^7	0.0411
1.2	4	1.60×10^8	12.7	1.25×10^8	0.0577
2.0	3	1.12×10^8	9.5	1.14×10^8	0.0683

3 Mathematical Model

In this work, we develop a thin-film model for colony biofilm growth, similar to those used by several authors [31, 34–36]. The base model considers colony biofilm growth along and perpendicular to a solid substratum of width X_s and depth H_s. The colony biofilm exists in the region $\Omega_b(t)$ bounded by $0 < x < S(t)$, and $0 < z < h(x,t)$, where $S(t)$ is the colony biofilm half-width, and $z = h(x,t)$ is the biofilm–air interface, which is a free surface. Inspired by Steinberg [59], we model cellular material and the EPS matrix as viscous fluids [60]. We partition the biomass into two phases, a living phase that contributes to growth and nutrient consumption, and an inactive phase of passive fluid. To incorporate the two phases into the model, we introduce the volume fractions of the living phase, $\phi_n(x,z,t)$, and the inactive phase, $\phi_m(x,z,t)$. In defining these volume fractions, we assume that an averaging process has occurred, as is standard in multiphase models [61]. The living biomass accounts for proliferating cells, and the inactive biomass phase represents dead cells. Since the proportion of cells to ECM in our experiments is unknown, we assume that both phases also contain extracellular fluid, such that the amount of ECM is proportional to the number of cells in each phase. The no-voids assumption, $\phi_n + \phi_m = 1$, applies throughout the domain.

The colony biofilm expands by cell proliferation and ECM production, driven by the consumption of nutrients supplied from the substratum. We assume that nutrients occupy no volume, and represent them as concentrations. We denote the nutrient concentration in the substratum as $g_s(x,z,t)$. This variable is defined in the substratum domain Ω_s, which is the fixed region bounded by $0 < x < X_s$ and $-H_s < z < 0$. During growth, the colony biofilm takes up nutrients from the substratum through the biofilm–substratum interface. We denote the nutrient concentration in the colony biofilm as $g_b(x,z,t)$, defined in $\Omega_b(t)$. A schematic illustrating the model geometry is shown in Figure 3.1.

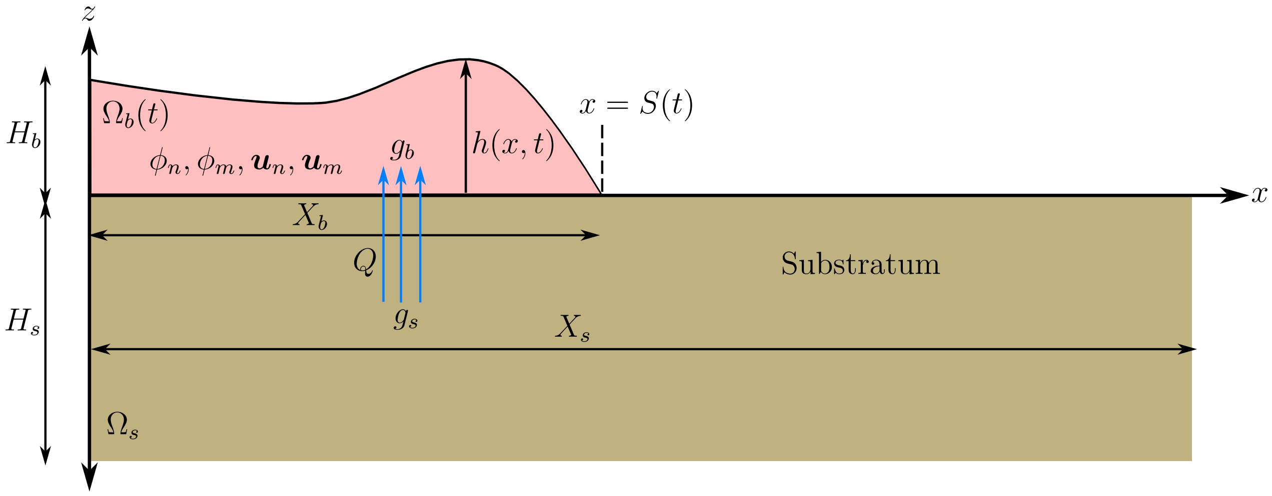

Figure 3.1: Schematic of the colony biofilm and agar geometry, showing the mathematical model variables. See the main text for the definitions of each symbol.

3.1 Governing Equations and Boundary Conditions

The model's governing equations arise from from mass and momentum conservation. Their derivation closely follows Tam et al. [36]. Here, we summarise the key assumptions, and we provide a detailed derivation in the Supporting Material. Cells catabolise glucose to facilitate cell proliferation, producing new biomass [62]. We adopt first-order kinetics to represent these processes. We assume that cell death occurs at a rate proportional to the volume fraction of living cells, which represents random accidental cell death. On death, we assume that cells immediately form part of the inactive phase, without any corresponding change in volume [31]. This assumption is consistent with the hypothesis that cell death influences the ECM composition [52]. We assume that nutrients disperse by diffusion in the substratum, and by diffusion and advection with both fluid phases in the colony biofilm, where they become available for consumption. Since yeast colony biofilms expand as a unit [12], we assume that there is large interphase drag [63–65], such that both fluid phases move with the common velocity $\boldsymbol{u} = (u, w)$.

On applying the model assumptions, we obtain mass balance equations for the volume fractions and nutrient concentrations. These are

$$
\begin{aligned}
\phi_n + \phi_m &= 1 && \text{in } \Omega_b(t), && (3.1\text{a})\\
\frac{\partial \phi_n}{\partial t} + \nabla \cdot (\phi_n \boldsymbol{u}) &= \psi_n \phi_n g_b - \psi_d \phi_n && \text{in } \Omega_b(t), && (3.1\text{b})\\
\frac{\partial \phi_m}{\partial t} + \nabla \cdot (\phi_m \boldsymbol{u}) &= \psi_d \phi_n && \text{in } \Omega_b(t), && (3.1\text{c})\\
\frac{\partial g_s}{\partial t} &= D_s \nabla^2 g_s && \text{in } \Omega_s, && (3.1\text{d})\\
\frac{\partial g_b}{\partial t} + \nabla \cdot (g_b \boldsymbol{u}) &= D_b \nabla^2 g_b - \eta \phi_n g_b && \text{in } \Omega_b(t), && (3.1\text{e})
\end{aligned}
$$

where $\nabla = (\partial_x, \partial_z)$, the parameter ψ_n is the biomass production rate, ψ_d is the cell death rate, D_s and D_b are the diffusivities of nutrients in the substratum and colony biofilm, respectively, and η is the nutrient consumption rate. To obtain the momentum balance equations, we assume that both phases are incompressible viscous Newtonian fluids [36] with a common pressure p and dynamic viscosity μ. Conservation of momentum for both phases then yields

$$
\nabla \cdot (\phi_\alpha \boldsymbol{\sigma}) + \boldsymbol{F}_\alpha = \boldsymbol{0} \quad \text{in } \Omega_b(t), \tag{3.2}
$$

where

$$
\boldsymbol{\sigma} = -\left(p + \frac{2\mu}{3} \nabla \cdot \boldsymbol{u}\right) \boldsymbol{I} + \mu \left[\nabla \boldsymbol{u} + (\nabla \boldsymbol{u})^T\right], \tag{3.3}
$$

is the Cauchy stress tensor, $\boldsymbol{F}_\alpha$ represents external sources of momentum for phase $\alpha = n, m$, and $\boldsymbol{I}$ is the identity tensor. For both fluid phases we neglect an explicit contribution to the pressure due to growth, instead assuming that material incompressibility drives expansion in response to cell proliferation [31, 36]. Since the velocity field is in general not divergence free, we include a bulk viscosity term in (3.3), with coefficient $-2\mu/3$ in accordance with Stokes' hypothesis [31, 36, 66, 67]. The momentum sources, $\boldsymbol{F}_\alpha$, are given explicitly by $\boldsymbol{F}_\alpha = -k(\boldsymbol{u}_n - \boldsymbol{u}_m) + p_\alpha \nabla \phi_\alpha$ for $\alpha = n, m$. These momentum sources consist of interphase drag and interfacial forces [36, 68–70]. Since we have assumed $\boldsymbol{u}_n = \boldsymbol{u}_m$, the drag component subsequently vanishes [63].

The boundary conditions include symmetry conditions for ϕ_n, ϕ_m, and u at $x = 0$, and no-flux conditions for the nutrient concentrations at the agar boundaries and the biofilm–air interface. We obtain another boundary condition by assuming that nutrients enter the colony biofilm at a rate proportional to the local concentration difference across the biofilm–substratum interface, neglecting osmotic effects. This yields the conditions

$$D_s \frac{\partial g_s}{\partial z} = D_b \frac{\partial g_b}{\partial z} = -Q\left(g_s - g_b\right) \quad \text{on} \quad z = 0, \tag{3.4}$$

where Q is a mass transfer coefficient describing the rate of nutrient uptake. We also apply standard boundary conditions from fluid mechanics, including no penetration on the biofilm–agar interface, and the kinematic condition and tangential and normal stress conditions on the biofilm–air free surface. Since sliding motility involves reduced surface tension [12], we neglect surface tension in the normal stress condition on the free surface. Surface tension in colony biofilms might represent the strength of cell–cell adhesion on the free surface [71]. In the work of Tam et al. [36], surface tension had minimal impact on horizontal expansion. The surface tension coefficient does affect the colony biofilm shape, and can inhibit ridge formation on the colony biofilm surface. Our experimental results do not contain ridges, and have similar profiles to the solutions of Tam et al. [36] with zero surface tension. Hence, we neglect surface tension in this work.

For the tangential stress balance on the biofilm–substratum interface, we impose a general slip condition, leading to

$$\mu \frac{\partial u}{\partial z} = \lambda u \quad \text{on} \quad z = 0, \tag{3.5}$$

where λ is a slip parameter representing the strength of biofilm–substratum adhesion. Whilst the general tangential stress condition (3.5) is was included in the models of Tam et al. [35] and Tam et al. [36], those works focused on the weak adhesion and perfect slip ($\lambda = 0$), and strong adhesion and no slip ($\lambda \to \infty$) scenarios, respectively. In this work, we consider the generalised case in which λ varies between these two limits, and estimate the value of λ using experimental data. This completes the system of governing equations and boundary conditions, a full description of which is available in the Supporting Material.

3.2 Extensional Flow Thin-Film Approximation

After establishing the mass and momentum balances, we simplify the governing equations using the thin-film approximation. We assume that the aspect ratios of the colony biofilm and agar substratum are equal, and exploit their thin geometries to write

$$\varepsilon = \frac{H_s}{X_s} = \frac{H_b}{X_b} \ll 1, \tag{3.6}$$

where H_b and X_b are the characteristic thickness and characteristic half-width of the colony biofilm, respectively. The characteristic colony biofilm thickness is chosen to be $H_b = X_b H_s / X_s$, which is not necessarily the initial colony biofilm thickness. The thin-film assumption is valid because the aspect ratio of the substratum in the experiments, $\varepsilon = H_s/X_s = 0.06$, lies within the aspect ratio range of mature colony biofilms (between 0.032 and 0.068 depending on agar density). We use the extensional flow scaling regime [31, 72]. This regime models yeast colony expansion by sliding motility [36], and produces more realistic colony biofilm shapes than the lubrication regime [35], which assumes higher pressure and surface tension. In extensional flows, the velocity is independent of z to leading order in ε, representing the scenario of weak biofilm–substratum adhesion. The nutrient concentrations are also z-independent to leading order in ε. Integrating the fluid volume fractions across z then yields a spatially one-dimensional model, in which all dependent variables are functions of x and t.

We adopt a nondimensionalisation based on the scaled variables

$$\begin{gathered} t = \frac{X_b^2}{D_b}\hat{t}, \quad (x, z) = \left(X_b\hat{x}, \varepsilon X_b \hat{z}\right), \quad (u, w) = \left(\frac{D_b}{X_b}\hat{u}, \frac{\varepsilon D_b}{X_b}\hat{w}\right), \\ g_s = G\hat{g}_s, \quad g_b = G\hat{g}_b, \quad \text{and} \quad p = \frac{\mu D_b}{X_b^2}\hat{p}, \end{gathered} \tag{3.7}$$

where G is the initial nutrient concentration in the substratum. After nondimensionalising and applying the thin-film approximation in the extensional flow regime, the dimensionless model to leading order in ε is the spatially one-dimensional system (dropping hats on leading order quantities)

$$\frac{\partial h}{\partial t} + \frac{\partial}{\partial x}(uh) = \Psi_n \phi g_b h \qquad \text{on} \quad 0 < x < S(t), \tag{3.8a}$$

$$\frac{\partial}{\partial t}(h\phi) + \frac{\partial}{\partial x}(uh\phi) = \Psi_n \phi g_b h - \Psi_d \phi h \qquad \text{on} \quad 0 < x < S(t), \tag{3.8b}$$

$$\frac{\partial g_s}{\partial t} = D\frac{\partial^2 g_s}{\partial x^2} - \delta Q^* \left(g_s - g_b\right) H(S(t) - x) \qquad \text{on} \quad 0 < x < 1/\delta, \tag{3.8c}$$

$$h\frac{\partial g_b}{\partial t} + \frac{\partial}{\partial x}(uhg_b) = \frac{\partial}{\partial x}\left(h\frac{\partial g_b}{\partial x}\right) + Q^*\left(g_s - g_b\right) - \Upsilon \phi g_b h \qquad \text{on} \quad 0 < x < S(t), \tag{3.8d}$$

$$4\frac{\partial}{\partial x}\left(h\frac{\partial u}{\partial x}\right) - \lambda^* u = 2\Psi_n \frac{\partial}{\partial x}(\phi g_b h) \qquad \text{on} \quad 0 < x < S(t), \tag{3.8e}$$

$$\frac{\mathrm{d}S}{\mathrm{d}t} = u(S(t), t), \tag{3.8f}$$

where $H(x)$ is the Heaviside step function. We include the Heaviside step function in (3.8c) because nutrient uptake only occurs where the colony biofilm is present. To leading order in ε, the dependent variables $h(x,t)$, $u(x,t)$, $g_s(x,t)$, $g_b(x,t)$, and $u(x,t)$ are z-independent. To obtain a spatially one-dimensional model, we introduce the depth-averaged cell volume fraction,

$$\phi(x,t) = \frac{1}{h}\int_0^h \phi_n(x,z,t)\,\mathrm{d}z, \tag{3.9}$$

which appears in the system (3.8). We use the no-voids condition (3.1a) to eliminate ϕ_m, which does not appear in (3.8). To close the model, we apply the initial conditions

$$g_s(x,0) = 1, \quad g_b(x,0) = 0, \quad \phi(x,0) = 0, \quad h(x,0) = H_0\left(1 - x^2\right), \quad S(0) = 1, \tag{3.10}$$

and boundary conditions,

$$\begin{gathered}
\left.\frac{\partial h}{\partial x}\right|_{(0,t)} = 0 \quad \left.\frac{\partial \phi}{\partial x}\right|_{(0,t)} = 0, \\
\left.\frac{\partial g_s}{\partial x}\right|_{(0,t)} = 0 \quad \left.\frac{\partial g_s}{\partial x}\right|_{(1/\delta,t)} = 0, \quad \left.\frac{\partial g_b}{\partial x}\right|_{(0,t)} = 0 \quad \left.\frac{\partial g_b}{\partial x}\right|_{(S(t),t)} = 0, \\
u(0,t) = 0, \quad \text{and} \quad \left.\frac{\partial u}{\partial x}\right|_{(S(t),t)} = \frac{1}{2}\Psi_n \phi(S(t),t) g_b(S(t),t).
\end{gathered} \tag{3.11}$$

A complete derivation of the system (3.8), (3.10) and (3.11) is available in the Supporting Material.

The dimensionless model (3.8), (3.10) and (3.11) contain 7 dimensionless parameters, defined in terms of dimensional quantities. These dimensionless parameters are

$$\begin{gathered}
\delta = \frac{X_b}{X_s}, \quad \Psi_n = \frac{G X_b^2 \psi_n}{D_b}, \quad \Psi_d = \frac{X_b^2 \psi_d}{D_b}, \quad D = \frac{D_s}{D_b}, \\
\Upsilon = \frac{X_b^2 \eta}{D_b}, \quad Q^* = \frac{X_b Q}{\varepsilon D_b}, \quad \text{and} \quad \lambda^* = \frac{X_b \lambda}{\varepsilon \mu}.
\end{gathered} \tag{3.12}$$

The parameter δ is the ratio of colony biofilm to Petri dish length scales. This parameter influences nutrient depletion from the substratum through Eqn. (3.8c), such that nutrients deplete more slowly on comparatively large substrates. The parameters Ψ_n and Ψ_d are the dimensionless biomass production and cell death rates, respectively, D is the nutrient diffusivity ratio, and Υ is the nutrient consumption rate. The parameters Q^* and λ^* are scaled to enter the leading order model through $\mathcal{O}(\varepsilon^2)$ corrections to the boundary conditions (see Supporting Material). The parameter Q^* is the nutrient uptake rate by the colony biofilm, and λ^* is the dimensionless adhesion strength. The adhesion strength parameter λ^* provides a drag-like term in the leading-order momentum equation (3.8e), such that increasing λ^* inhibits expansion. Parameter estimation will predict that the dimensionless quantities (3.12) are of $\mathcal{O}(1)$ size, indicating that the extensional flow scaling is suitable.

An advantage of our two-phase moving-boundary model is that it enables comparison with new experimental data for the colony biofilm composition, expansion speed, and aspect ratio. We compute numerical solutions of the model (3.8), (3.10) and (3.11), and compare the results with our experiments. We obtain numerical solutions to the mathematical model (3.8), (3.10) and (3.11) using a front-fixing transformation and the Crank–Nicolson method, similar to Tam et al. [36]. Full details of the numerical scheme are available in the Supporting Material, and open source JULIA code is available on GitHub.

3.3 Model Parameters

Table 3.1 contains parameter values used throughout this work. The agar density, agar depth, amount of nutrient, duration, and Petri dish dimensions are known from the experiments. We also obtain estimates for the nutrient diffusivities from the literature, yielding estimates for D_s [73, 74] and D_b [75]. In the extensional flow regime, the colony biofilm expansion speed depends on the initial condition [31, 36]. If the nutrient supply and the cell volume fraction are held constant, Ward and King [31] showed that the colony biofilm profile evolves to a travelling wave with speed proportional to $1/H_0$ as $t \to \infty$, where H_0 is the initial dimensionless colony biofilm thickness. Consequently, the dimensional parameter H_0 will impact expansion speed, and subsequently the comparison between the model and experiments. Although we have no reliable way to measure H_0 in the experiments, all experiments were inoculated in the same way. Therefore, we expect H_0 to be constant across all replicates, and to not vary with agar density. In the experiments, cells were applied to the agar using the tip of an inoculating loop of 4.5 mm diameter, such that $X_b \approx 2\,\mathrm{mm}$. The inoculum is a thin streak of cells and fluid that is rapidly absorbed into the agar layer. The cell density of this initial streak is much less than the cell density once the colony biofilm develops [76]. Consequently, we set $H_0 = 6\,\mu\mathrm{m}$, which is an upper estimate for the minor axis diameter of a single cell of Σ1278b *S. cerevisiae* yeast [15, 77, 78].

We still require values for the biomass production rate ψ_n, cell death rate ψ_d, nutrient uptake coefficient Q, nutrient consumption rate η, and the slip coefficient λ. Since cellular behaviour and/or properties of the agar determine these parameters, they are difficult to directly measure in experiments. We also hypothesise that these parameters might depend on the agar density. Therefore, we seek new estimates for the values of ψ_n, ψ_d, Q, η, and λ for each agar density, a. We cannot adopt the parameter values of Tam et al. [36], whose experiments were performed solely on 0.3% agar. Instead, we obtain parameter estimates by fitting the model to experimental data, as described in Section 4.1. Differences in these parameters between experiments on different agar densities will indicate how the agar density impacts colony biofilm growth.

Table 3.1: Estimated values for dimensional parameters in the mathematical model.

Parameter	**Symbol**	**Value(s)**	**Units**	**Source(s)**
Agar density (weight percentage)	a	$\{0.6, 0.8, 1.2, 2.0\}$	–	Experiment
Experimental duration	T	30780	min	Experiment
Petri dish half-width	X_s	50	mm	Experiment
Agar depth	H_s	3	mm	Experiment
Initial biofilm half-width	X_b	2	mm	Experiment
Initial biofilm thickness	H_0	0.006	mm	[15, 77, 78]
Initial nutrient concentration	G	1.5×10^{-4}	$\mathrm{g\,mm^{-2}}$	Experiment
Nutrient diffusivity (water)	D_0	4.04×10^{-2}	$\mathrm{mm^2\,min^{-1}}$	[73]
Nutrient diffusivity (substratum)	D_s	$(1-0.023a)D_0$	$\mathrm{mm^2\,min^{-1}}$	[74]
Nutrient diffusivity (biofilm)	D_b	$0.24D_0$	$\mathrm{mm^2\,min^{-1}}$	[75]

4 Results and Discussion

We use numerical solutions and optimisation to fit five unknown parameters to experimental data on different density growth media. We obtain good fits to expansion speed, colony biofilm composition, and aspect ratio data. This approach reveals a stronger impact of nutrient limitation on softer agar, and increased biofilm–substratum adhesion on harder agar. A combination of sensitivity analysis and synthetic data suggests that the increase in biofilm–substratum adhesion is the most robust difference between the agar densities.

4.1 Parameter Estimation

We use a numerical optimisation method to obtain point estimates for the model parameters that correspond to experiments. Holding some parameters constant across all agar densities as per Table 3.1, we obtain one set of optimal parameters $\theta^*(a) = (\Psi_n(a), \Psi_d(a), Q^*(a), \Upsilon(a), \lambda^*(a))$ for each of the four agar densities used in our experiments. The dimensional quantities X_b, G, D_b, ε, and μ are independent of the agar density. Our parameter estimates are based on minimising the difference between the experimental data and a numerical solution to the mathematical model. To perform the comparison, we introduce three summary statistics, $\mathcal{S}_S$, $\mathcal{S}_\Phi$, and $\mathcal{S}_A$. These statistics are the L^2-norms of the relative differences in half-width, composition, and aspect ratio, respectively, between the model solution with parameters θ and the experiments on agar density a. Their definitions are

$$\mathcal{S}_S(\theta, a) = \sqrt{\sum_{j=1}^{8} \left[\frac{S(t_j;\theta) - \bar{S}(t_j, a)}{\bar{S}(t_j, a)} \right]^2}, \tag{4.1a}$$

$$\mathcal{S}_\Phi(\theta, a) = \sqrt{\sum_{k=1}^{3} \left[\frac{\phi_n(x_k, t^*;\theta) - \Phi_k}{\Phi_k} \right]^2}, \tag{4.1b}$$

$$\mathcal{S}_A(\theta, a) = \frac{1}{A(a)} \left| \frac{\max_x \varepsilon h(x, t^*;\theta)}{S(t^*)} - A(a) \right|, \tag{4.1c}$$

where

$$\bar{S}(t_j, a) = \frac{1}{N} \sum_{i=1}^{N} S_i(t_j; a), \tag{4.2}$$

is the half-width averaged over the N experimental replicates, and t^* refers to the appropriate (dimensionless) time at which the experimental measurement was taken. Based on these summary statistics (4.1), we define the distance metric

$$\rho(\theta, a) = \sqrt{\mathcal{S}_S^2 + \mathcal{S}_\Phi^2 + \mathcal{S}_A^2}, \tag{4.3}$$

which provides a single measure of the difference between the model and experiments. Using the relative difference for each statistic (4.1) means that half-width, composition, and aspect ratio will have similar weighting when calculating ρ. The optimal parameter values for agar density a are then

$$\theta^*(a) = \underset{\theta}{\operatorname{argmin}}\, \rho(\theta, a), \tag{4.4}$$

which is the set of parameters that minimises the distance between the model solution and experimental data.

To establish a procedure for computing the optimal parameter set $\theta^*(a)$ numerically, we use optimisation packages available in JULIA. Once we have chosen the agar density for which to obtain parameter estimates, the optimisation procedure is as follows:

1. We obtained a coarse estimate, $\theta_0^*(a)$, using the Differential Evolution method with adaptive weights [79, 80], as implemented in the global optimisation package `BlackBoxOptim.jl`. We terminate the black box optimisation after 100 function evaluations, where one function evaluation refers to a computation of $\rho(\theta, a)$, which involves solving the PDE model (3.8), (3.10) and (3.11) for a set of parameters θ, and computing $\mathcal{S}_S$, $\mathcal{S}_\Phi$, and $\mathcal{S}_A$. The black box step provides a good initial guess for gradient-based optimisation. Increasing the number of function evaluations

beyond 100 had negligible effect on the results.

2. Using $\theta_0^*(a)$ as the initial guess, we use the LBFGS [81–84] method in `Optim.jl` [85] to estimate $\theta^*(a)$. Where necessary, we approximate the gradient $\nabla_\theta \rho$ numerically using first-order finite differencing, and use the Hager–Zhang line search [86]. We apply box constraints to ensure that all parameters are positive, with 3 outer iterations, and absolute tolerances of $\varepsilon = 1 \times 10^{-6}$ for the objective function and the L^∞-norm of the minimiser.

Repeated application of the optimisation procedure to the same experimental data yielded only minor differences in the minimiser $\theta^*(a)$. Therefore, on each run our gradient-based optimisation method converges effectively to a global minimum in ρ. Since each evaluation of the objective function $\rho(\theta, a)$ requires solving the model numerically once, the parameter estimation procedure is computationally expensive. In this work, we present all results using $N_\xi = 101$ grid points and $N_\tau = 401$ for consistency, as the computational cost for large-scale results becomes prohibitive for finer resolutions. Although the quantitative results at this resolution are grid-dependent, the qualitative conclusions reported herein remain valid as the numerical grid is refined. Further information regarding grid convergence is available in the Supporting Material. The optimal set of dimensionless parameters found for each value of the agar density are presented in Table 4.1. We obtained a good fit to experimental data for all agar densities. The accuracy of the fit is illustrated in Figure 4.1, where the colony biofilm size over time predicted numerically closely matches the experiments.

Table 4.1: Numerical solutions for the optimal set of dimensionless parameters, $\theta^*(a)$, for each agar density. The presented parameter values are the mean values from 5 repetitions of the optimisation routine, with the numerical solutions having been computed using $N_\xi = 101$ grid points and $N_\tau = 401$ time steps.

a	Ψ_n	Ψ_d	Q^*	Υ	λ^*	$\rho(\theta^*, a)$
0.6	0.301	0.00777	7.56	7.87	0.670	0.0437
0.8	0.365	0.00747	6.55	7.33	1.041	0.0536
1.2	0.409	0.00755	4.48	6.46	1.848	0.0636
2.0	0.302	0.00835	3.27	5.01	2.671	0.0625

The optimal biomass production and death rates, Ψ_n and Ψ_d, only vary slightly with changing agar density. These results reaffirm that proliferation and death rates are cell-associated properties with minimal dependence on the substratum. In contrast, Q^*, Υ, and λ^* vary more significantly with agar density. The nutrient uptake rate decreases with increasing agar hardness. He et al. [56] reported a similar result in *E. coli* bacteria. Since nutrient availability depends on both the uptake and

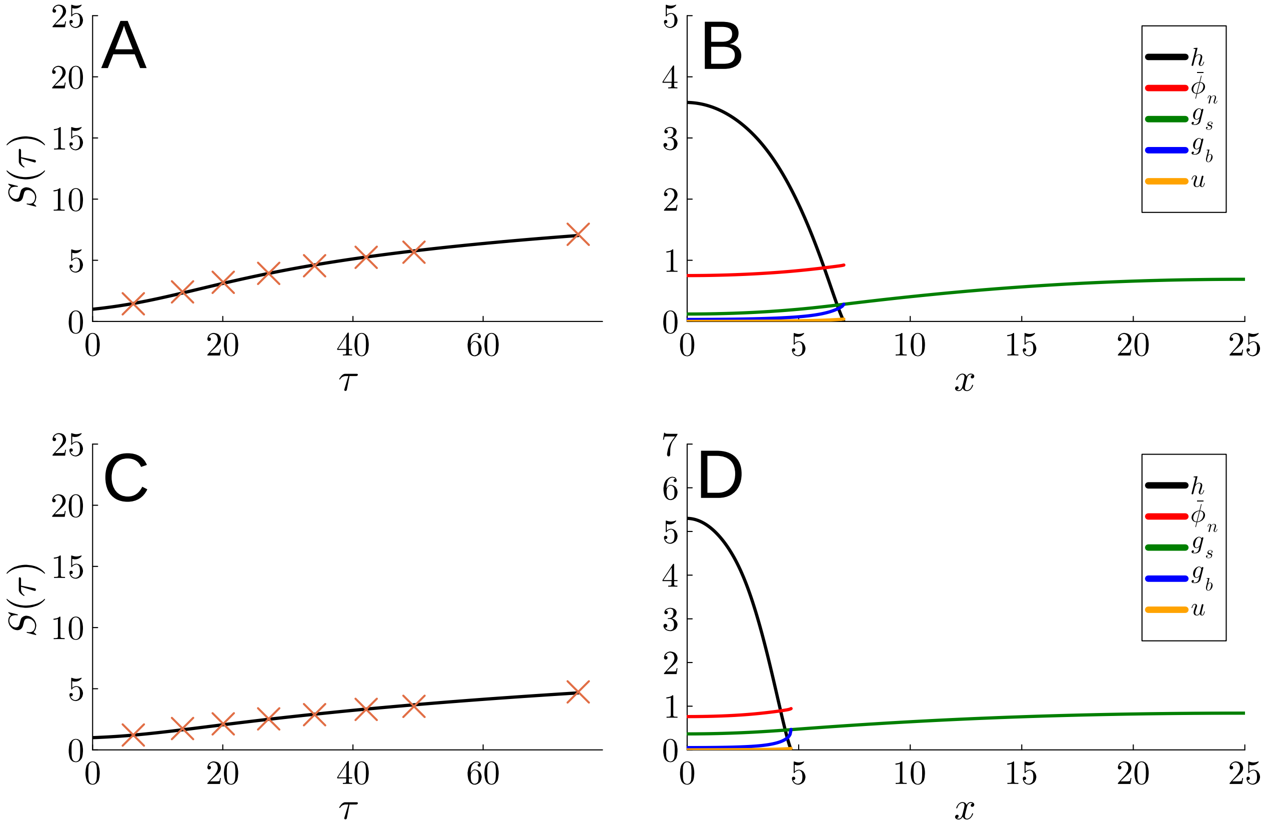

Figure 4.1: Numerical solutions to the mathematical model (3.8), (3.10) and (3.11) with the estimated parameters from Table 4.1, for both soft (0.6%) and hard (2.0%) agar. The numerical solutions were computed using $N_\xi = 101$ grid points and $N_\tau = 401$ time steps. (A) Comparison between model solution (black curve) and experimental data (orange crosses) for the dimensionless colony biofilm size, $S(\tau)$, on 0.6% agar. (B) Numerical solution for $\tau = 74.6$, corresponding to Day 21 of the experiment, using optimal parameters for 0.6% agar. (C) Comparison between model solution (black curve) and experimental data (orange crosses) for the dimensionless colony biofilm size, $S(\tau)$, on 2.0% agar. (D) Numerical solution for $\tau = 74.6$, corresponding to Day 21 of the experiment, using optimal parameters for 2.0% agar.

consumption rate, the decrease in nutrient uptake is accompanied by a smaller decrease in nutrient consumption rate, Υ. The higher Q^* and Υ values indicate that nutrients deplete faster for colonies grown on softer agar. This depletion could also be due to agar dehydration or osmotic effects, which we neglect in the model. The most striking effect is the increase in the dimensionless adhesion strength, λ^*, with increasing agar density. The small value of λ^* on 0.6% agar suggests that the perfect slip approximation ($\lambda^* = 0$) may be suitable for very soft agar. This supports the use of perfect slip by Tam et al. [36], whose experiments were on 0.3% media. The slip coefficient becomes more important on harder agar. The increased λ^* on harder substrates increases drag-like friction, inhibiting horizontal expansion [87, 88] relative to vertical expansion. This explains the thicker colony biofilm profiles on harder agar. Similar behaviour in *E. coli* was also reported by He et al. [56], and this prediction aligns with the recent experimental results of Pokhrel et al. [55]. Given the potential for biological variability across experiments, we perform a series of analyses to assess the robustness of the results to changes in each parameter.

4.2 Uncertainty and Sensitivity Analyses

Our experimental results consist of relatively few replicates that are subject to biological variation. We perform a series of analyses to determine the robustness of the parameter estimation results presented in Section 4.1. First, we investigate how varying the model parameters influences $\rho(\theta, a)$, the global distance metric that compares the mathematical model solution and experimental data. We present these results in the parameter-pair heat maps for 0.6% agar in Figure 4.2. In this figure, we vary parameters two at a time from zero to approximately three times their optimal values, holding the other parameters constant at their optimal values. The parameter-pair heat maps show the computed values of $\rho(\theta, a)$ as two parameters are varied.

The biomass production rate, Ψ_n, has a narrow band of values that yield small values of $\rho(\theta, a)$. Increasing Ψ_n increases $S(t)$ in numerical solutions [36]. Varying Ψ_n from its optimal value causes large changes in ρ, suggesting that Ψ_n strongly influences the solutions and is well-identified by the experimental data. Compared to Ψ_n, varying Ψ_d has a smaller impact on the size of ρ. This is because cell death rate has a lesser effect on expansion speed [36], and only significantly impacts the living cell volume fraction, ϕ. Since colony biofilm composition had minimal variation with agar density in our experiments, the optimal value for Ψ_d remains similar across all agar densities considered.

Compared to other parameters, the distance $\rho(\theta, a)$ is also less sensitive to the nutrient uptake rate, Q^*. In the model, nutrients taken up from the substratum do not occupy volume, and therefore only

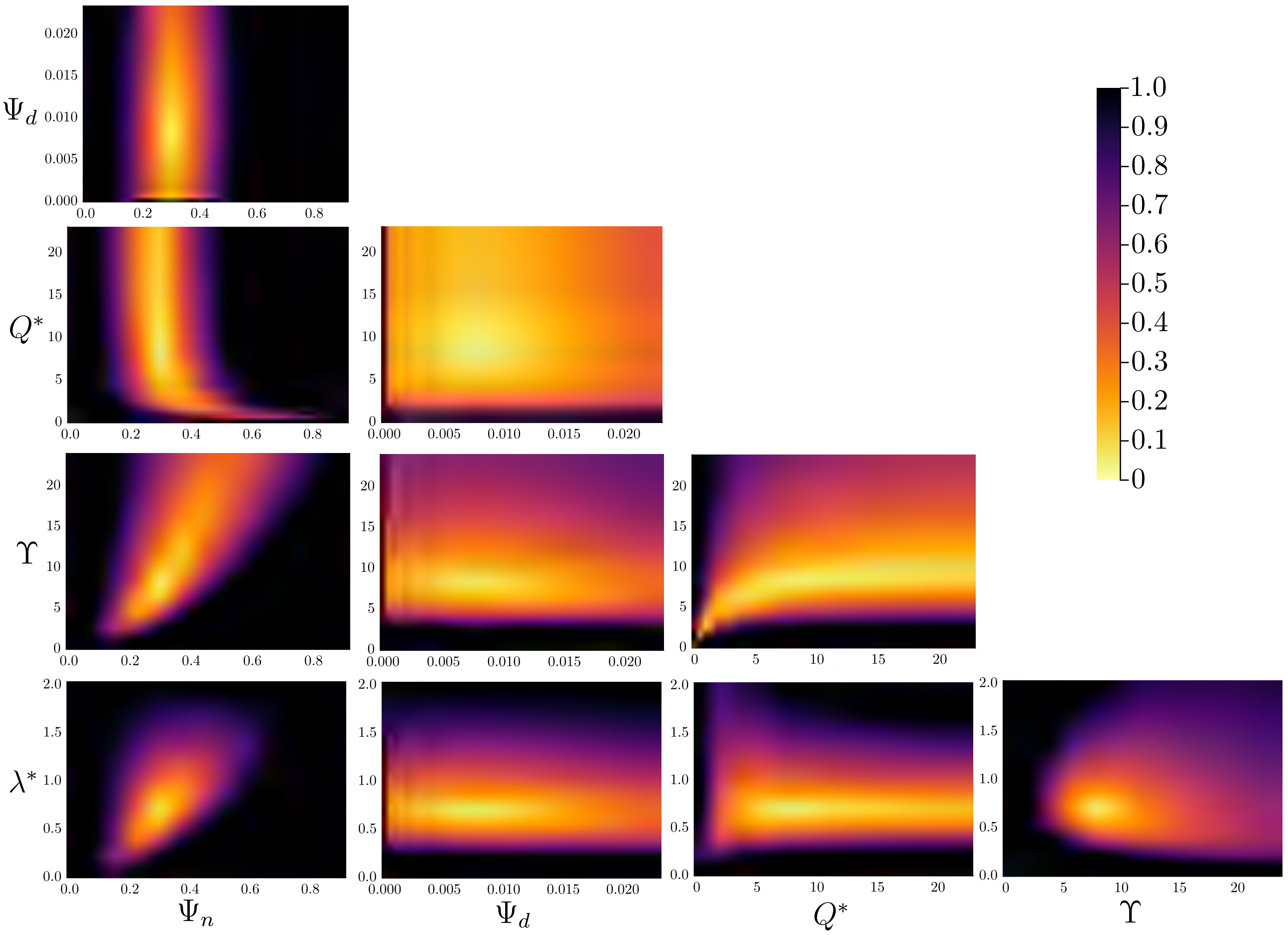

Figure 4.2: Parameter-pair heat maps for soft (0.6%) agar. Each plot shows the value of the global distance metric, $\rho(\theta, a)$, for a given set of parameters. Unless otherwise stated, all parameters take the optimal values listed in Table 4.1. When varied, each parameter ranges from zero to three times the optimal value (2,500 total simulations).

contribute to growth when consumed. Nutrient consumption in the colony biofilm is influenced by both the uptake rate, Q^*, and consumption rate, Υ. Consequently, there is a range of pairs (Q^*, Υ) that yield good fits to the data. Therefore, although our procedure identifies differences in Q^* and Υ across agar densities, the parameter Q^* is less well-identified than Ψ_n. A future version of the model that accounts for volumetric increase due to nutrient uptake, for example by osmotic swelling, could shed further light on the importance of nutrient uptake.

Increasing the biofilm–substratum adhesion strength λ^* increases the aspect ratio and decreases horizontal expansion [35]. Consequently, this parameter is well identified, with a comparatively narrower range of values yielding small $\rho(\theta, a)$. Since the aspect ratio increases with agar hardness, so too does the optimal adhesion strength λ^*. Taken together, this parameter-pair analysis reveals the key roles of the biomass production rate, nutrient consumption, and cell–substratum adhesion in determining the colony biofilm size and shape.

To investigate uncertainties in our parameter estimates further, we infer optimal parameter sets from individual experimental replicates, rather than from the mean of all experiments of a given agar density. These results are presented in Table 4.2, which reveal that the quantitative trends persist across different replicates of the same agar density.

Table 4.2: Optimal parameters for all individual experimental replicates.

a	Rep.	Ψ_n	Ψ_d	Q^*	Υ	λ^*	$\rho(\theta^*, a)$
0.6	1	0.299	0.00778	7.68	7.82	0.666	0.0446
	2	0.306	0.00778	6.84	8.01	0.691	0.0460
	3	0.312	0.00771	7.58	7.63	0.653	0.0448
	4	0.290	0.00780	8.10	8.02	0.674	0.0405
0.8	1	0.363	0.00762	5.94	6.35	0.973	0.0537
	2	0.312	0.00787	6.99	6.51	0.982	0.0451
	3	0.378	0.00731	6.84	8.27	1.107	0.0555
	4	0.416	0.00709	6.89	8.64	1.119	0.0590
1.2	1	0.380	0.00783	3.89	5.67	1.806	0.0629
	2	0.392	0.00766	4.50	6.09	1.785	0.0619
	3	0.429	0.00743	4.54	6.89	1.904	0.0652
	4	0.434	0.00731	5.13	7.21	1.883	0.0640
2.0	1	0.301	0.00835	3.26	5.01	2.681	0.0620
	2	0.236	0.00919	3.27	5.62	2.357	0.0510
	3	0.404	0.00757	3.59	7.37	3.088	0.0723

To supplement these results and account for experimental variability further, we repeated the optimisation procedure using synthetic data. For the synthetic aspect ratio data, we generated a synthetic cell count from a normal distribution with the mean and standard deviation from experiments, and computed the corresponding aspect ratio following the method outlined in Section 2.2. To generate synthetic half-width data $S(t_j; a)$, we sampled once from the standard normal distribution, $z \sim \mathcal{N}(0, 1)$, and set $S(t_j; a) = \bar{S}(t_j; a) + z\sigma(t_j; a)$ where $\bar{S}(t_j, a) = (\sum_{i=1}^{n} S_i(t_j; a))/n$ are the mean measurements at each time point, and $\sigma(t_j; a)$ is the standard deviation. For the synthetic colony biofilm composition data, we scaled Φ_k by the same random number drawn from a uniform distribution $U(0.932, 1.05)$, which allows for composition results across the range observed in experiments. We generated 50 sets of synthetic data for each agar density, and obtained an optimal parameter set for each data set. The variability in these optimal parameters is shown in Figure 4.3.

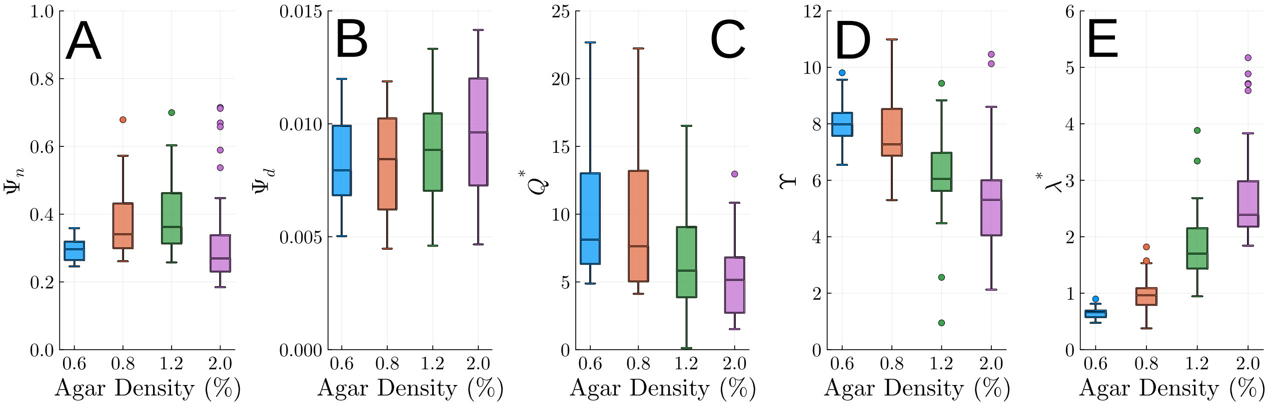

Figure 4.3: Box plots representing the optimal parameter values found using our parameter estimation procedure for 50 synthetic experiments on each agar density. Circle markers indicate outliers. (A) Ψ_n. (B) Ψ_d. (C) Q^*. (D) Υ. (E) λ^*.

For a fixed agar density, the optimal biomass production rates Ψ_n and cell death rates Ψ_d vary. This result demonstrates the variability across synthetic replicates. However, as expected both parameters do not depend strongly on agar density. Some studies have predicted increased cell death with increasing adhesion strength [89, 90]. Although we predict slightly higher values of Ψ_d on harder agar, we cannot reliably conclude that agar density affects Ψ_d in yeast from our available data. Our parameter estimates in Table 4.1 indicate that the nutrient uptake rate Q^* and nutrient consumption rate Υ both decrease with increasing agar density. Although agar hardness is thought to inhibit nutrient uptake in bacteria such as *E. coli* [56], we find wide variability in Q^* across the synthetic experiments. This finding is consistent with the parameter pair heat maps in Figure 4.2, where Q^* was a difficult parameter to identify. The decreasing trend in Υ with agar density is more robust than the trend in Q^*, but is still subject to significant variability. Of all parameters, the biofilm–substratum adhesion strength λ^* has the strongest variation with agar density in synthetic experiments, and the least variability across synthetic replicates. These results provide further evidence that agar density mediates friction between the colony biofilm and substratum in *S. cerevisiae* colony biofilms.

A characteristic of extensional flows is that the expansion speed depends on the initial condition [31, 36]. Since the functional form of $\mathcal{H}(x)$ and the initial thickness H_0 are unknown, we also investigate the effect of the initial thickness, H_0, on the results. Varying the initial thickness between zero and three *S. cerevisiae* cells thick reveals that the distance $\rho(\theta, a)$ is relatively insensitive to H_0, compared to other parameters. This is especially true for $H_0 \geq 0.05$, which is the dimensionless thickness of a single yeast cell. Therefore, the differences between replicates are unlikely to be due to experimental variations in H_0. These results are presented in Figure 4.4.

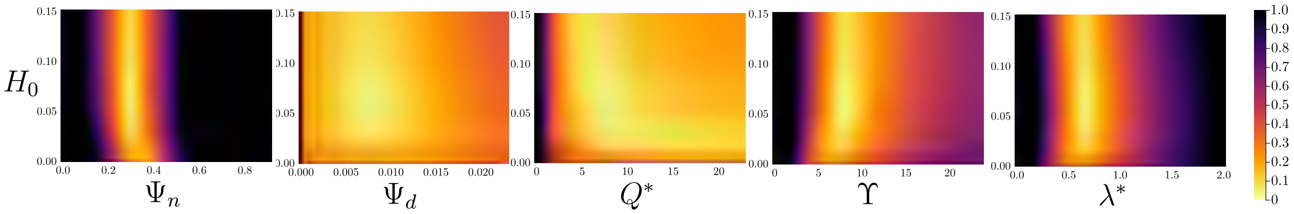

Figure 4.4: Parameter pair heat maps for the initial thickness, H_0, on 0.6% agar. Plots represent the distance between the numerical solution and experimental data, $\rho(\theta, a)$, for given parameter combination. Unless otherwise stated, parameters take the optimal values. When varied, each parameter ranges from zero to three times the optimal value (2,500 total simulations).

5 Conclusion

In this manuscript, we have combined *S. cerevisiae* experiments and mathematical modelling to quantify how agar density and cell death impact yeast colony biofilm growth. Our experimental method extended previous mat formation experiments [7–9] to incorporate rectangular geometry, colony biofilm composition measurements, and aspect ratio measurements. We adapted the thin-film extensional flow model of Tam et al. [36] to include cell death and resistance to slip caused by biofilm–substratum adhesion. Using new experimental data from multiple experiments, we estimated model parameters for four agar densities. The strongest impact of increasing agar hardness was to increase the biofilm–substratum adhesion strength, measured through the parameter λ^*. This finding is consistent with previous studies in bacteria, suggesting that increased adhesion with agar hardness is a general phenomenon of microbial growth. There was also a decrease in nutrient uptake and consumption rates on harder agar. These effects have also been hypothesised or observed in bacteria. However, parameter sensitivity analysis and synthetic data yielded wider variability in the nutrient uptake rate and consumption parameters compared to biofilm–substratum adhesion. The biomass production and death rates were consistent across agar densities.

Our mathematical model is based on the principle that the colony biofilm constituents can be modelled as viscous fluids [59]. Provided that this assumption is valid, the model describes the mechanics of colony biofilm growth due to biomass proliferation, mediated by a depleting nutrient supply. Although the slip parameter λ^* quantifies the drag due to biofilm–substratum adhesion, it does not provide a full description of the substratum mechanics. The agar may dehydrate over time [56], and colony biofilm attachment to the substratum may exert forces that deform the agar [54]. Our cross-sectional photographs of the colony biofilm indicate that these deformations might be small, but we neglect such deformations in the model. To confirm that agar deformation does not alter our main conclusions, a possible extension to the model could be to incorporate the agar mechanics explicitly. This would complicate the analysis significantly, as one would need to incorporate constitutive relations for the material properties of the agar, and continuity of stress on the biofilm–substratum interface, which may also change shape over time. This extension is left for future work. A further extension for future work is to incorporate osmotic swelling, which influences bacterial biofilm expansion [32–34]. Despite evidence that osmotic stresses indeed affect individual *S. cerevisiae* cells [91], the phenomenon of osmotic swelling in yeast colony biofilms is not widely reported. Osmotic influx from the substratum would contribute to volumetric growth of the colony biofilm, and nutrient supply. If significant, it would introduce new parameters to the model and alter the estimates of existing parameters. Another avenue for future investigation is to understand the non-uniform front pattern that often develops at later times, as shown in Figure 2.1. The amplitude of this pattern decreases on harder agar, and future work could focus on understanding how nutrient availability and agar density affect these interfacial instabilities.

Fungal biofilms are notorious for their ability to colonise indwelling medical devices [92, 93], and are a leading cause of hospital-acquired infections [94–97]. Our cross-sectional images reveal that a small number of yeast cells invade the agar medium in our experiments. Although the continuum model used in this paper does not permit invasion, invasive growth of yeast is important in clinical settings, because invasion of healthy tissue leads to the spread of infections [98]. Modelling the biophysics of yeast cell invasion is a problem for future work. Other colony biofilm experiments have featured a region of dead cells close to the leading edge. This region is thought to appear due to cells undergoing regulated cell death [22]. We neglected regulated cell death in this work, because our colony biofilms instead have regions of cell death near their inoculation site, reminiscent of a necrotic core [99, 100] formed by accidental cell death. Since regulated cell death is known to occur in yeast colony biofilms, fully characterising the roles of accidental and regulated cell death [51], and their relationship to mechanics, remains an open question. In addition to multiple types of cell death, future work could also involve applying the multi-phase model to multi-species colony biofilms, which more closely resemble those in healthcare environments. Natural and artificial surfactants can disrupt biofilm growth in wounds and hasten their removal [101]. Whilst this effect is irrelevant to sliding motility where surface tension is negligible, it provides another promising avenue for future modelling work as researchers continue to explore the wide range of yeast growth modes, and strategies for eliminating biofilms.

Acknowledgements

We acknowledge funding from the Australian Research Council (Grant numbers DP230100406, and DE240100097).

Authorship Contribution Statement

- **AKYT:** Conceptualisation, methodology, software, validation, formal analysis, investigation, data curation, writing – original draft, writing – review & editing, visualisation, funding acquisition.
- **DJN:** Conceptualisation, formal analysis, writing – review & editing.
- **JMG:** Methodology, investigation, data curation, writing – original draft.
- **JZ:** Methodology, investigation, data curation.
- **CWG:** Conceptualisation, funding acquisition.
- **VJ:** Resources, writing – review & editing, supervision, funding acquisition.
- **BJB:** Conceptualisation, writing – review & editing, project administration, funding acquisition.
- **JEFG:** Conceptualisation, writing – review & editing, supervision, funding acquisition.

Competing Interests

We have no competing interests to declare.

Data Availability

Open source JULIA code and experimental photographs used to generate the results in this paper is available on GitHub.

References

[1] J. W. Costerton, P. S. Stewart, and E. P. Greenberg, "Bacterial Biofilms: A Common Cause of Persistent Infections", *Science* 284 (1999), pp. 1318–1322, DOI: 10.1126/science.284.5418.1318.

[2] J. R. Blankenship and A. P. Mitchell, "How to Build a Biofilm: A Fungal Perspective", *Curr. Opin. Microbiol.* 9 (2006), pp. 588–594, DOI: 10.1016/j.mib.2006.10.003.

[3] P. Stoodley, K. Sauer, D. G. Davies, and J. W. Costerton, "Biofilms as Complex Differentiated Communities", *Annu. Rev. Microbiol.* 56 (2002), pp. 187–209, DOI: 10.1146/annurev.micro.56.012302.160705.

[4] D. Botstein, S. A. Chervitz, and M. Cherry, "Yeast as a Model Organism", *Science* 277 (1997), pp. 1259–1260, DOI: 10.1126/science.277.5330.1259.

[5] R. K. Bojsen, K. S. Andersen, and B. Regenberg, "*Saccharomyces cerevisiae* — a Model to Uncover Molecular Mechanisms for Yeast Biofilm Biology", *FEMS Immunol. Med. Microbiol.* 65 (2012), pp. 169–182, DOI: 10.1111/j.1574-695X.2012.00943.x.

[6] A. Goffeau, B. G. Barrell, H. Bussey, R. W. Davis, B. Dujon, H. Feldmann, F. Galibert, J. D. Hoheisel, C. Jacq, M. Johnston, E. J. Louis, H. W. Mewes, Y. Murakami, P. Philippsen, H. Tettelin, and S. G. Oliver, "Life with 6000 Genes", *Science* 274 (1996), pp. 546–567, DOI: 10.1126/science.274.5287.546.

[7] T. B. Reynolds and G. R. Fink, "Bakers' Yeast, a Model for Fungal Biofilm Formation", *Science* 291 (2001), pp. 878–881, DOI: 10.1126/science.291.5505.878.

[8] A. Tam, J. E. F. Green, S. Balasuriya, E. L. Tek, J. M. Gardner, J. F. Sundstrom, V. Jiranek, and B. J. Binder, "Nutrient-Limited Growth with Non-Linear Cell Diffusion as a Mechanism for Floral Pattern Formation in Yeast Biofilms", *J. Theor. Biol.* 448 (2018), pp. 122–141, DOI: 10.1016/j.jtbi.2018.04.004.

[9] E. L. Tek, J. F. Sundstrom, J. M. Gardner, S. G. Oliver, and V. Jiranek, "Evaluation of the Ability of Commercial Wine Yeasts to Form Biofilms (Mats) and Adhere to Plastic:

Implications for the Microbiota of the Winery Environment", *FEMS Microbiol. Ecol.* 94 (2018), fix188, DOI: 10.1093/femsec/fix188.

[10] T. B. Reynolds, A. Jansen, X. Peng, and G. R. Fink, "Mat Formation in *Saccharomyces cerevisiae* Requires Nutrient and pH Gradients", *Eukaryotic Cell* 7 (2008), pp. 122–130, DOI: 10.1128/ec.00310-06.

[11] J. Recht, A. Martínez, S. Torello, and R. Kolter, "Genetic Analysis of Sliding Motility in *Mycobacterium smegmatis*", *J. Bacteriol.* 182 (2000), pp. 4348–4351, DOI: 10.1128/JB.182.15.4348-4351.2000.

[12] R. M. Harshey, "Bacterial Motility on a Surface: Many Ways to a Common Goal", *Annu. Rev. Microbiol.* 57 (2003), pp. 249–273, DOI: 10.1146/annurev.micro.57.030502.091014.

[13] M. R. Mattei, L. Frunzo, B. D'Acunto, Y. Pechaud, F. Pirozzi, and G. Esposito, "Continuum and Discrete Approach in Modeling Biofilm Development and Structure: A Review", *J. Math. Biol.* 76 (2018), pp. 945–1003, DOI: 10.1007/s00285-017-1165-y.

[14] I. Klapper and J. Dockery, "Mathematical Description of Microbial Biofilms", *SIAM Rev.* 52 (2010), pp. 221–265, DOI: 10.1137/080739720.

[15] K. Li, J. E. F. Green, H. Tronnolone, A. K. Y. Tam, A. J. Black, J. M. Gardner, J. F. Sundstrom, V. Jiranek, and B. J. Binder, "An Off-Lattice Discrete Model to Characterise Filamentous Yeast Colony Morphology", *PLoS Comput. Biol.* 20 (2024), e1012605, DOI: 10.1371/journal.pcbi.1012605.

[16] C. Picioreanu, M. C. M. van Loosdrecht, and J. J. Heijnen, "Mathematical Modeling of Biofilm Structure with a Hybrid Differential-Discrete Cellular Automaton Approach", *Biotechnol. Bioeng.* 58 (1998), pp. 101–116, DOI: 10.1002/(SICI)1097-0290(19980405)58:1<101::AID-BIT11>3.0.CO;2-M.

[17] S. Matsuura, "Random Growth of Fungal Colony Model on Diffusive and Non-Diffusive Media", *Forma* 15 (2000), pp. 309–319.

[18] H. Tronnolone, J. M. Gardner, J. F. Sundstrom, V. Jiranek, S. G. Oliver, and B. J. Binder, "TAMMiCol: Tool for Analysis of the Morphology of Microbial Colonies", *PLoS Comput. Biol.* 14 (2018), e1006629, DOI: 10.1371/journal.pcbi.1006629.

[19] K. Kawasaki, A. Mochizuki, M. Matsushita, T. Umeda, and N. Shigesada, "Modeling Spatio-Temporal Patterns Generated by *Bacillus subtilis*", *J. Theor. Biol.* 188 (1997), pp. 177–185, DOI: `10.1006/jtbi.1997.0462`.

[20] B. F. Gray and N. A. Kirwan, "Growth Rates of Yeast Colonies on Solid Media", *Biophys. Chem.* 1 (1974), pp. 204–213, DOI: `10.1016/0301-4622(74)80006-2`.

[21] P. Ghosh and H. Levine, "Morphodynamics of a Growing Microbial Colony Driven by Cell Death", *Phys. Rev. E* 96 (2017), p. 052404, DOI: `10.1103/PhysRevE.96.052404`.

[22] D. J. Netherwood, A. K. Y. Tam, C. W. Gourlay, T. Knežević, J. M. Gardner, V. Jiranek, B. J. Binder, and J. E. F. Green, "Accidental and Regulated Cell Death in Yeast Colony Biofilms", *Bull. Math. Biol.* 87 (2025), 110, DOI: `10.1101/2025.02.02.636168`.

[23] E. Ben-Jacob, I. Cohen, and H. Levine, "Cooperative Self-Organization of Microorganisms", *Adv. Phys.* 49 (2000), pp. 395–554, DOI: `10.1080/000187300405228`.

[24] L. Chen, J. Noorbakhsh, R. M. Adams, J. Samaniego-Evans, G. Agollah, D. Nevozhay, J. Kuzdzal-Fick, P. Mehta, and G. Balázsi, "Two-Dimensonality of Yeast Colony Expansion Accompanied by Pattern Formation", *PLoS Comput. Biol.* 10 (2014), e1003979, DOI: `10.1371/journal.pcbi.1003979`.

[25] J. Müller and W. van Saarloos, "Morphological Instability and Dynamics of Fronts in Bacterial Growth Models with Nonlinear Diffusion", *Phys. Rev. E* 65 (2002), 061111, DOI: `10.1103/PhysRevE.65.061111`.

[26] K. A. Rahman, R. Sudarsan, and H. J. Eberl, "A Mixed-Culture Biofilm Model with Cross-Diffusion", *Bull. Math. Biol.* 77 (2015), pp. 2086–2124, DOI: `10.1007/s11538-015-0117-1`.

[27] A. Gallegos, B. Mazzag, and A. Mogilner, "Two Continuum Models for the Spreading of Myxobacteria Swarms", *Bull. Math. Biol.* 68 (2006), pp. 837–861, DOI: `10.1007/s11538-005-9031-2`.

[28] C. Giverso, M. Verani, and P. Ciarletta, "Branching Instability in Expanding Bacterial Colonies", *J. R. Soc. Interface* 12 (2015), 20141290, DOI: `10.1098/rsif.2014.1290`.

[29] C. Fei, S. Mao, J. Yan, R. Alert, H. A. Stone, B. L. Bassler, N. S. Wingreen, and A. Košmrlj, "Nonuniform Growth and Surface Friction Determine Bacterial Biofilm

Morphology on Soft Substrates", *Proc. Natl. Acad. Sci. U.S.A.* 117 (2020), pp. 7622–7632, DOI: 10.1073/pnas.1919607117.

[30] J. P. Ward, J. R. King, A. J. Koerber, J. M. Croft, R. E. Sockett, and P. Williams, "Early Development and Quorum Sensing in Bacterial Biofilms", *J. Math. Biol.* 47 (2003), pp. 23–55, DOI: 10.1007/s00285-002-0190-6.

[31] J. P. Ward and J. R. King, "Thin-Film Modelling of Biofilm Growth and Quorum Sensing", *J. Eng. Math.* 73 (2012), pp. 71–92, DOI: 10.1007/s10665-011-9490-4.

[32] A. Seminara, T. E. Angelini, J. N. Wilking, H. Vlamakis, S. Ebrahim, R. Kolter, D. A. Weitz, and M. P. Brenner, "Osmotic Spreading of *Bacillus subtilis* Biofilms Driven by an Extracellular Matrix", *Proc. Natl. Acad. Sci. U.S.A.* 109 (2012), pp. 1116–1121, DOI: 10.1073/pnas.1109261108.

[33] J. Yan, C. D. Nadell, H. A. Stone, N. S. Wingreen, and B. L. Bassler, "Extracellular-Matrix-Mediated Osmotic Pressure Drives *Vibrio cholerae* Biofilm Expansion and Cheater Exclusion", *Nat. Commun.* 8 (2017), 327, DOI: 10.1038/s41467-017-00401-1.

[34] S. Srinivasan, C. N. Kaplan, and L. Mahadevan, "A Multiphase Theory for Spreading Microbial Swarms and Films", *eLife* 8 (2019), e42697, DOI: 10.7554/eLife.42697.

[35] A. K. Y. Tam, B. Harding, J. E. F. Green, S. Balasuriya, and B. J. Binder, "Thin-Film Lubrication Model for Biofilm Expansion under Strong Adhesion", *Phys. Rev. E* 105 (2022), 014408, DOI: 10.1103/PhysRevE.105.014408.

[36] A. Tam, J. E. F. Green, S. Balasuriya, E. L. Tek, J. M. Gardner, J. F. Sundstrom, V. Jiranek, and B. J. Binder, "A Thin-Film Extensional Flow Model for Biofilm Expansion by Sliding Motility", *Proc. Royal Soc. A* 475 (2019), 20190175, DOI: 10.1098/rspa.2019.0175.

[37] M. P. Brenner, "Fluid Mechanical Responses to Nutrient Depletion in Fungi and Biofilms", *Phys. Fluids* 26 (2014), 101306, DOI: 10.1063/1.4896587.

[38] A. Persat, C. D. Nadell, M. K. Kim, F. Ingremeau, A. Siryaporn, K. Drescher, N. S. Wingreen, B. L. Bassler, Z. Gitai, and H. A. Stone, "The Mechanical World of Bacteria", *Cell* 161 (2015), pp. 988–997, DOI: 10.1016/j.cell.2015.05.005.

[39] H. F. Winstanley, M. Chapwanya, M. J. McGuinness, and A. C. Fowler, “A Polymer–Solvent Model of Biofilm Growth”, *Proc. Royal Soc. A* 467 (2010), pp. 1449–1467, DOI: 10.1098/rspa.2010.0327.

[40] J. Lega and T. Passot, “Hydrodynamics of Bacterial Colonies: A Model”, *Phys. Rev. E* 67 (2003), 031906, DOI: 10.1103/physreve.67.031906.

[41] N. G. Cogan and R. D. Guy, “Multiphase Flow Models of Biogels from Crawling Cells to Bacterial Biofilms”, *Front. Life Sci.* 4 (2010), pp. 11–25, DOI: 10.2976/1.3291142.

[42] F. Clarelli, C. Di Russo, R. Natalini, and M. Ribot, “A Fluid Dynamics Multidimensional Model of Biofilm Growth: Stability, Influence of Environment and Sensitivity”, *Math. Med. Biol.* 33 (2015), pp. 371–395, DOI: 10.1093/imammb/dqv024.

[43] M. Asally, M. Kittisopikul, P. Rué, Y. Du, Z. Hu, T. Çağatay, A. B. Robinson, H. Lu, J. Garcia-Ojalvo, and G. M. Süel, “Localized Cell Death Focuses Mechanical Forces during 3D Patterning in a Biofilm”, *Proc. Natl. Acad. Sci. U.S.A.* 109 (2012), pp. 18891–18896, DOI: 10.1073/pnas.1212429109.

[44] O. Wanner and W. Gujer, “A Multispecies Biofilm Model”, *Biotechnol. Bioeng.* 28 (1986), pp. 314–328, DOI: 10.1002/bit.260280304.

[45] H. J. Eberl, D. F. Parker, and M. C. M. van Loosdrecht, “A New Deterministic Spatio-Temporal Continuum Model for Biofilm Development”, *J. Theor. Med.* 3 (2001), pp. 161–175, DOI: 10.1080/10273660108833072.

[46] S. Trinschek, K. John, and U. Thiele, “From a Thin Film Model for Passive Suspensions towards the Description of Osmotic Biofilm Spreading”, *AIMS Mater. Sci.* 3 (2016), pp. 1138–1159, DOI: 10.3934/matersci.2016.3.1138.

[47] S. Trinschek, K. John, S. Lecuyer, and U. Thiele, “Continuous versus Arrested Spreading of Biofilms at Solid–Gas Interfaces: The Role of Surface Forces”, *Phys. Rev. Lett.* 119 (2017), 078003, DOI: 10.1103/PhysRevLett.119.078003.

[48] S. Trinschek, K. John, and U. Thiele, “Modelling of Surfactant-Driven Front Instabilities in Spreading Bacterial Colonies”, *Soft Matter* 14 (2018), pp. 4464–4476, DOI: 10.1039/c8sm00422f.

[49] G. T. Fortune, N. M. Oliveira, and R. E. Goldstein, "Biofilm Growth under Elastic Confinement", *Phys. Rev. Lett.* 128 (2022), 178102, DOI: 10.1103/PhysRevLett.128.178102.

[50] P. Bravo, S. L. Ng, K. A. MacGillivray, B. K. Hammer, and P. J. Yunker, "Vertical Growth Dynamics of Biofilms", *Proc. Natl. Acad. Sci. U.S.A.* 120 (2023), e2214211120, DOI: 10.1073/pnas.2214211120.

[51] D. Carmona-Gutierrez, M. A. Bauer, A. Zimmermann, A. Aguilera, N. Austriaco, K. Ayscough, R. Balzan, S. Bar-Nun, A. Barrientos, P. Belenky, M. Blondel, R. J. Braun, M. Breitenbach, W. C. Burhans, S. Büttner, D. Cavalieri, M. Chang, K. F. Cooper, M. Côrte-Real, V. Costa, C. Cullin, I. Dawes, J. Dengjel, M. B. Dickman, T. Eisenberg, B. Fahrenkrog, N. Fasel, K. U. Fröhlich, A. Gargouri, S. Giannattasio, P. Goffrini, C. W. Gourlay, C. M. Grant, M. T. Greenwood, N. Guaragnella, T. Heger, J. Heinisch, E. Herker, J. M. Herrmann, S. Hofer, A. Jiménez-Ruiz, H. Jungwirth, K. Kainz, D. P. Kontoyiannis, P. Ludovico, S. Manon, E. Martegani, C. Mazzoni, L. A. Megeney, C. Meisinger, J. Nielsen, T. Nyström, H. D. Osiewacz, T. F. Outeiro, H. Park, T. Pendl, D. Petranovic, S. Picot, P. Polčic, T. Powers, M. Ramsdale, M. Rinnerthaler, P. Rockenfeller, C. Ruckenstuhl, R. Schaffrath, M. Segovia, F. F. Severin, A. Sharon, S. J. Sigrist, C. Sommer-Ruck, M. J. Sousa, J. M. Thevelein, K. Thevissen, V. Titorenko, M. B. Toledano, M. Tuite, F. N. Vögtle, B. Westermann, J. Winderickx, S. Wissing, S. Wölfl, Z. J. Zhang, R. Y. Zhao, B. Zhou, L. Galluzzi, G. Kroemer, and F. Madeo, "Guidelines and Recommendations on Yeast Cell Death Nomenclature", *Microb. Cell* 5 (2018), pp. 4–31, DOI: 10.15698/mic2018.01.607, PMID: 29354647.

[52] Z. Palková and L. Váchová, "Cell Differentiation, Aging, and Death in Spatially Organized Yeast Communities: Mechanisms and Consequences", *Cell Death Differ.* (2025), pp. 1–13, DOI: 10.1038/s41418-025-01485-9.

[53] M. Čáp, L. Štěpánek, K. Harant, L. Váchová, and Z. Palková, "Cell Differentiation within a Yeast Colony: Metabolic and Regulatory Parallels with a Tumor-Affected Organism", *Mol. Cell* 46 (2012), pp. 436–448, DOI: 10.1016/j.molcel.2012.04.001, PMID: 22560924.

[54] A. Pietz, K. John, and U. Thiele, “The Role of Substrate Mechanics in Osmotic Biofilm Spreading”, *Soft Matter* 21 (2025), pp. 2935–2945, DOI: 10.1039/D4SM01463D.

[55] A. R. Pokhrel, R. Copeland, M. Hejri, T. E. R. Belpaire, G. Steinbach, S. L. Ng, B. K. Hammer, and P. J. Yunker, *Cell-Substrate Friction Controls Biofilm Development*, 2025, DOI: 10.1101/2025.07.11.664457, pre-published.

[56] C. He, L. Han, D. C. Harris, S. Bayakhmetov, X. Wang, and Y. Kuang, “Reaction–Diffusion Modeling of *E. coli* Colony Growth Based on Nutrient Distribution and Agar Dehydration”, *Bull. Math. Biol.* 85 (2023), p. 61, DOI: 10.1007/s11538-023-01163-2.

[57] W. J. Middelhoven, B. Broekhuizen, and J. van Eijk, “Detection, with the Dye Phloxine B, of Yeast Mutants Unable to Utilize Nitrogenous Substances as the Sole Nitrogen Source”, *J. Bacteriol.* 128 (1976), pp. 851–852, DOI: 10.1128/jb.128.3.851-852.1976.

[58] J. F. Cannon, J. B. Gibbs, and K. Tatchell, “Supperssors of the Ras2 Mutation of *Saccharomyces cerevisiae*”, *Genetics* 113 (1986), pp. 247–264, DOI: 10.1093/genetics/113.2.247.

[59] M. S. Steinberg, “Reconstruction of Tissues by Dissociated Cells”, *Science* 141 (1963), pp. 401–408, DOI: 10.1126/science.141.3579.401.

[60] I. Klapper, C. J. Rupp, R. Cargo, B. Purvedorj, and P. Stoodley, “Viscoelastic Fluid Description of Bacterial Biofilm Material Properties”, *Biotechnol. Bioeng.* 80 (2002), pp. 289–296, DOI: 10.1002/bit.10376.

[61] D. A. Drew, “Mathematical Modeling of Two-Phase Flow”, *Annu. Rev. Fluid Mech.* 15 (1983), pp. 261–291, DOI: 10.1146/annurev.fl.15.010183.001401.

[62] J. Maršíková, D. Wilkinson, O. Hlaváček, G. D. Gilfillan, A. Mizeranschi, T. R. Hughes, M. Begany, S. Rešetárová, L. Váchová, and Z. Palková, “Metabolic Differentiation of Surface and Invasive Cells of Yeast Colony Biofilms Revealed by Gene Expression Profiling”, *BMC Genom.* 18 (2017), 814, DOI: 10.1186/s12864-017-4214-4.

[63] R. D. O’Dea, S. L. Waters, and H. M. Byrne, “A Two-Fluid Model for Tissue Growth within a Dynamic Flow Environment”, *Eur. J. Appl. Math.* 19 (2008), pp. 607–634, DOI: 10.1017/S0956792508007687.

[64] S. J. Franks, H. M. Byrne, J. R. King, J. C. E. Underwood, and C. E. Lewis, "Modelling the Early Growth of Ductal Carcinoma in situ of the Breast", *J. Math. Biol.* 47 (2003), pp. 424–452, DOI: 10.1007/s00285-003-0214-x.

[65] S. R. Lubkin and T. L. Jackson, "Multiphase Mechanics of Capsule Formation in Tumors", *J. Biomech. Eng.* 124 (2002), pp. 237–243, DOI: 10.1115/1.1427925.

[66] S. J. Franks and J. R. King, "Interactions between a Uniformly Proliferating Tumour and Its Surroundings: Uniform Material Properties", *Math. Med. Biol.* 20 (2003), pp. 47–89, DOI: 10.1093/imammb/20.1.47.

[67] R. D. O'Dea, S. L. Waters, and H. M. Byrne, "A Multiphase Model for Tissue Construct Growth in a Perfusion Bioreactor", *Math. Med. Biol.* 27 (2010), pp. 95–127, DOI: 10.1093/imammb/dqp003.

[68] D. A. Drew and L. A. Segel, "Averaged Equations for Two-Phase Flows", *Stud. Appl. Math.* 50 (1971), pp. 205–231, DOI: 10.1002/sapm1971503205.

[69] G. Lemon, J. R. King, H. M. Byrne, O. E. Jensen, and K. M. Shakesheff, "Mathematical Modelling of Engineered Tissue Growth Using a Multiphase Porous Flow Mixture Theory", *J. Math. Biol.* 52 (2006), pp. 571–594, DOI: 10.1007/s00285-005-0363-1.

[70] J. E. F. Green, J. P. Whiteley, J. M. Oliver, H. M. Byrne, and S. L. Waters, "Pattern Formation in Multiphase Models of Chemotactic Cell Aggregation", *Math. Med. Biol.* 35 (2017), pp. 319–346, DOI: 10.1093/imammb/dqx005.

[71] G. Forgacs, R. A. Foty, Y. Shafrir, and M. S. Steinberg, "Viscoelastic Properties of Living Embryonic Tissues: A Quantitative Study", *Biophys. J.* 74 (1998), pp. 2227–2234, DOI: 10.1016/S0006-3495(98)77932-9.

[72] P. D. Howell, B. Scheid, and H. A. Stone, "Newtonian Pizza: Spinning a Viscous Sheet", *J. Fluid Mech.* 659 (2010), pp. 1–23, DOI: 10.1017/S0022112010001564.

[73] L. G. Longsworth, "Diffusion in Liquids and the Stokes–Einstein Relation", *Electrochemistry in Biology and Medicine*, ed. by T. Shedlovsky, First edition, New York: John Wiley & Sons, Ltd, 1955, pp. 225–247.

[74] A. L. Slade, A. E. Cremers, and H. C. Thomas, "The Obstruction Effect in the Self-Diffusion Coefficients of Sodium and Cesium in Agar Gels", *J. Phys. Chem.* 70 (1966), pp. 2840–2844, DOI: 10.1021/j100881a020.

[75] P. S. Stewart, “A Review of Experimental Measurements of Effective Diffusive Permeabilities and Effective Diffusion Coefficients in Biofilms”, *Biotechnol. Bioeng.* 59 (1998), pp. 261–272, DOI: 10.1002/(SICI)1097-0290(19980805)59:3<261::AID-BIT1>3.0.CO;2-9.

[76] A. Tam, “Mathematical Modelling of Pattern Formation in Yeast Biofilms”, PhD thesis, The University of Adelaide, 2019, HDL: 2440/122613.

[77] C. J. Gimeno, P. O. Ljungdahl, C. A. Styles, and G. R. Fink, “Unipolar Cell Divisions in the Yeast *S. cerevisiae* Lead to Filamentous Growth: Regulation by Starvation and RAS”, *Cell* 68 (1992), pp. 1077–1090, DOI: 10.1016/0092-8674(92)90079-R.

[78] M. Zakhartsev and M. Reuss, “Cell Size and Morphological Properties of Yeast *Saccharomyces cerevisiae* in Relation to Growth Temperature”, *FEMS Yeast Res.* 18 (2018), foy052, DOI: 10.1093/femsyr/foy052.

[79] R. M. Storn and K. V. Price, “Differential Evolution – a Simple and Efficient Heuristic for Global Optimization over Continuous Spaces”, *J. Glob. Optim.* 11 (1997), pp. 341–359, DOI: 10.1023/A:1008202821328.

[80] K. V. Price, R. M. Storn, and J. A. Lampinen, *Differential Evolution: A Practical Approach to Global Optimization*, Natural Computing Series, Berlin/Heidelberg: Springer-Verlag, 2005, ISBN: 978-3-540-20950-8, DOI: 10.1007/3-540-31306-0.

[81] C. G. Broyden, “The Convergence of a Class of Double-Rank Minimization Algorithms 1. General Considerations”, *IMA J. Appl. Math.* 6 (1970), pp. 76–90, DOI: 10.1093/imamat/6.1.76.

[82] R. Fletcher, “A New Approach to Variable Metric Algorithms”, *Comput. J.* 13 (1970), pp. 317–322, DOI: 10.1093/comjnl/13.3.317.

[83] D. Goldfarb, “A Family of Variable-Metric Methods Derived by Variational Means”, *Math. Comp.* 24 (1970), pp. 23–26, DOI: 10.1090/S0025-5718-1970-0258249-6.

[84] D. F. Shanno, “Conditioning of Quasi-Newton Methods for Function Minimization”, *Math. Comp.* 24 (1970), pp. 647–656, DOI: 10.1090/S0025-5718-1970-0274029-X.

[85] P. K. Mogensen and A. N. Risbeth, “Optim: A Mathematical Optimization Package for Julia”, *J. Open Source Softw.* 3 (2018), 615, DOI: 10.21105/joss.00615.

[86] W. W. Hager and H. Zhang, "Algorithm 851: CG_DESCENT, a Conjugate Gradient Method with Guaranteed Descent", *ACM Trans. Math. Softw.* 32 (2006), pp. 113–137, DOI: 10.1145/1132973.1132979.

[87] M. L. Stecchini, M. Del Torre, S. Donda, E. Maltini, and S. Pacor, "Influence of Agar Content on the Growth Parameters of *Bacillus cereus*", *Int. J. Food Microbiol.* 64 (2001), pp. 81–88, DOI: 10.1016/S0168-1605(00)00436-0.

[88] R. Ziege, A. Tsirigoni, B. Large, D. O. Serra, K. G. Blank, R. Hengge, P. Fratzl, and C. M. Bidan, "Adaptation of *Escherichia coli* Biofilm Growth, Morphology, and Mechanical Properties to Substrate Water Content", *ACS Biomater. Sci. Eng.* 7 (2021), pp. 5315–5325, DOI: 10.1021/acsbiomaterials.1c00927.

[89] L. Z. Y. Huang, Z. L. Shaw, R. Penman, S. Cheeseman, V. K. Truong, M. J. Higgins, R. A. Caruso, and A. Elbourne, "Cell Adhesion, Elasticity, and Rupture Forces Guide Microbial Cell Death on Nanostructured Antimicrobial Titanium Surfaces", *ACS Appl. Bio Mater.* 7 (2024), pp. 344–361, DOI: 10.1021/acsabm.3c00943.

[90] S. Desai, K. Sanghrajka, and D. Gajjar, "High Adhesion and Increased Cell Death Contribute to Strong Biofilm Formation in *Klebsiella pneumoniae*", *Pathogens* 8 (4 2019), p. 277, DOI: 10.3390/pathogens8040277.

[91] G. J. Morris, L. Winters, G. E. Coulson, and K. J. Clarke, "Effect of Osmotic Stress on the Ultrastructure and Viability of the Yeast *Saccharomyces cerevisiae*", *Microbiology* 132 (1986), pp. 2023–2034, DOI: 10.1099/00221287-132-7-2023.

[92] E. M. Kojic and R. O. Darouiche, "*Candida* Infections of Medical Devices", *Clin. Microbiol. Rev.* 17 (2004), pp. 255–267, DOI: 10.1128/cmr.17.2.255-267.2004.

[93] L. M. Martinez and B. C. Fries, "Fungal Biofilms: Relevance in the Setting of Human Disease", *Curr. Fungal Infect. Rep.* 4 (2010), pp. 266–275, DOI: 10.1007/s12281-010-0035-5.

[94] C. J. Nobile and A. D. Johnson, "*Candida albicans* Biofilms and Human Disease", *Annu. Rev. Microbiol.* 69 (2015), pp. 71–92, DOI: 10.1146/annurev-micro-091014-104330.

[95] G. Ramage, R. Rajendran, L. Sherry, and C. Williams, "Fungal Biofilm Resistance", *Int. J. Microbiol.* 2012 (2012), 528521, DOI: 10.1155/2012/528521.

[96] P. G. Pappas, M. S. Lionakis, M. C. Arendrup, L. Ostrosky-Zeichner, and B. J. Kullberg, “Invasive Candidiasis”, *Nat. Rev. Dis. Primers* 4 (2018), 18026, DOI: `10.1038/nrdp.2018.26`.

[97] M. S. Lionakis, “New Insights into Innate Immune Control of Systemic Candidiasis”, *Med. Mycol.* 52 (2014), pp. 555–564, DOI: `10.1093/mmy/myu029`.

[98] P. J. Cullen and G. F. Sprague, “Glucose Depletion Causes Haploid Invasive Growth in Yeast”, *Proc. Natl. Acad. Sci. U.S.A.* 97 (2000), pp. 13619–13624, DOI: `10.1073/pnas.240345197`.

[99] H. P. Greenspan, “Models for the Growth of a Solid Tumor by Diffusion”, *Stud. Appl. Math.* 51 (1972), pp. 317–340, DOI: `10.1002/sapm1972514317`.

[100] H. M. Byrne and M. A. J. Chaplain, “Modelling the Role of Cell-Cell Adhesion in the Growth and Development of Carcinomas”, *Math. Comput. Model.* 24 (1996), pp. 1–17, DOI: `10.1016/s0895-7177(96)00174-4`.

[101] S. L. Percival, D. Mayer, R. S. Kirsner, G. Schultz, D. Weir, S. Roy, A. Alavi, and M. Romanelli, “Surfactants: Role in Biofilm Management and Cellular Behaviour”, *Int. Wound J.* 16 (2019), pp. 753–760, DOI: `10.1111/iwj.13093`.

Supporting Material: Quantifying the effects of cell death and agar density on yeast colony biofilms using an extensional flow mathematical model

Alexander K. Y. Tam[1,*], Daniel J. Netherwood[2], Jennifer M. Gardner[3], Jin Zhang[3], Campbell W. Gourlay[4], Vladimir Jiranek[3,5], Benjamin J. Binder[2], and J. Edward F. Green[2]

[1]UniSA STEM, The University of South Australia, Mawson Lakes SA 5095, Australia

[2]School of Computer and Mathematical Sciences, The University of Adelaide, Adelaide SA 5005, Australia

[3]Department of Wine Science, School of Agriculture, Food and Wine, The University of Adelaide, Glen Osmond SA 5064, Australia

[4]Kent Fungal Group, School of Biosciences, The University of Kent, Canterbury, Kent, United Kingdom

[5]School of Biological Sciences, The University of Southampton, Southampton, United Kingdom

[*]Correspondence: alex.tam@unisa.edu.au

Contents

A Experimental Results

A.1 Experimental Photographs and Image Processing

Figure A.1 illustrates a time series of photographs for one replicate of colony biofilm growth on each agar density. We used photographs to obtain experimental measurements of the colony biofilm half-width. To achieve this, we imported the photograph using Julia's `FileIO` and `Images` packages. We then converted the photograph to a binary image using Otsu's method. An example binary image is shown in Figure A.2.

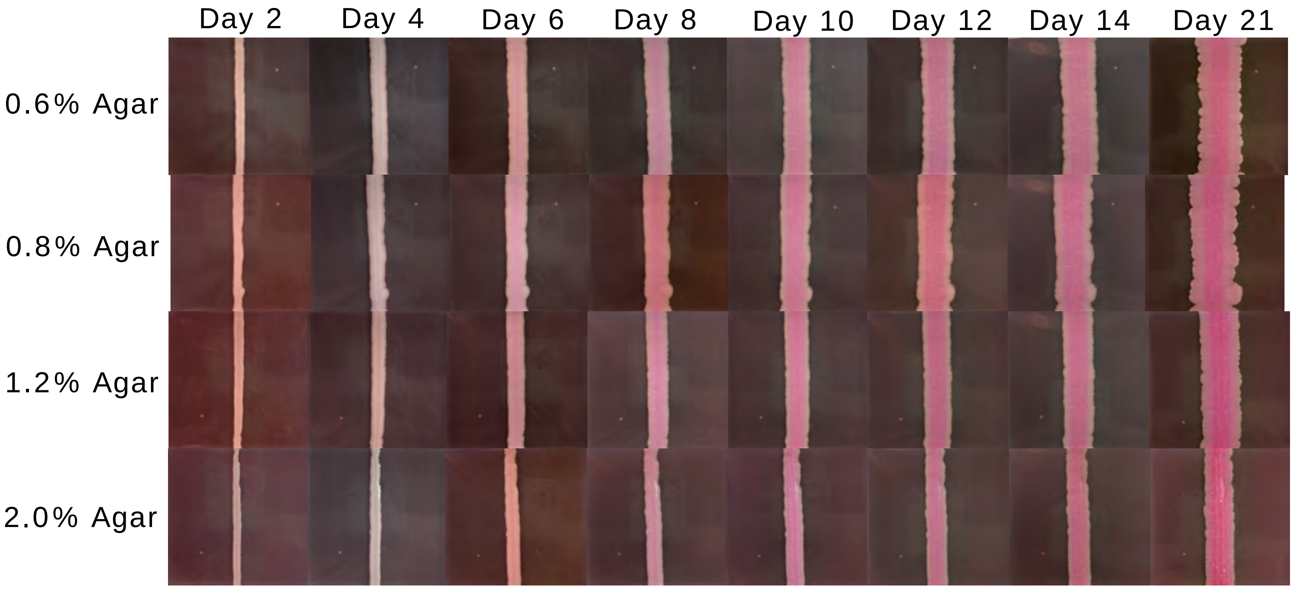

Figure A.1: Time series of cropped photographs for one replicate of colony biofilm growth on each agar density.

(a) Experiment.

(b) Binary image.

Figure A.2: (a) Experimental photograph for replicate 2 on 0.8% agar, after 21 days of growth. (b) Corresponding binary image obtained using Otsu's method.

After binarisation, we computed the total number of occupied (white) pixels in the largest connected component in the binary image, which will be the colony biofilm. Then, we divided by the height (in pixels) of the image to obtain the mean colony biofilm width, in pixels. Using a ruler placed next to the Petri dish (not shown in Figure A.2), we then determined the physical width of a pixel in each photograph. This allowed us to convert the mean colony biofilm width in pixels to a half-width in physical units. Repeating this process on all experimental photographs yielded $S(t)$ for each experimental replicate. We used the standard deviation in $S(t)$ across all replicates of the same agar density when generating synthetic data, as described in the main manuscript.

A.2 Cell Counts

The cell count data was collected by sampling from a $4\,\mathrm{cm}^2$ region of the colony biofilms on Day 21. The collection regions were rectangles with dimensions $4\,\mathrm{cm} \times 1\,\mathrm{cm}$, the blue boxes in Figure A.3. After sampling, cells were counted using a hemocytometer and a Nikon Eclipse 50i microscope. The total cell counts and the standard deviations are shown in Table A.1.

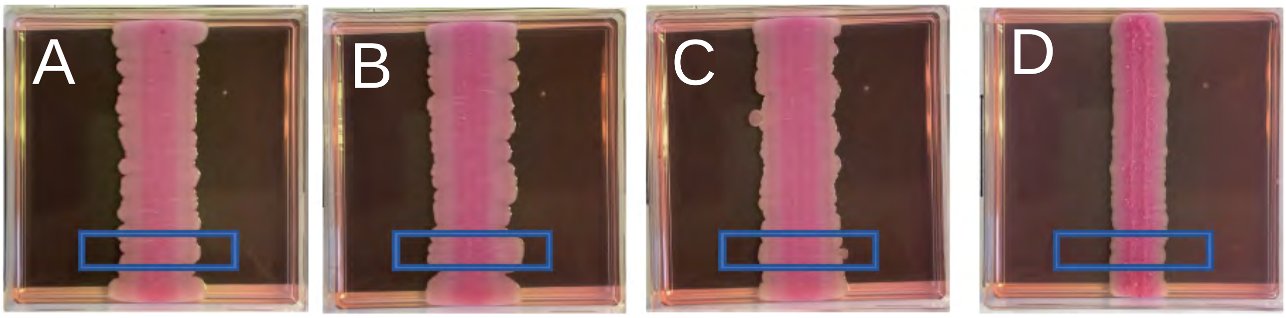

Figure A.3: Colony biofilm photographs on Day 21 indicating the regions (blue box) from which the cell count samples were collected. (A) 0.6% agar. (B) 0.8% agar. (C) 1.2% agar. (D) 2.0% agar.

Although the cell counts were taken from a $4\,\mathrm{cm}^2$ region for each colony biofilm, the sampled area of the colony biofilm varies with agar density, because the colony biofilm half-width $S(t)$ varies with agar density. The cell counts presented in the main manuscript represent the average number of cells across the region of width $S(t)$ in the x-direction, per millimetre in the y-direction. This cell number then provided a way to estimate the colony biofilm height, which we converted to an aspect ratio because $S(t)$ was known. For the synthetic data, we generated a random cell count by sampling from a normal distribution with mean and standard deviation as

Table A.1: Experimental cell count data from Day 21 of yeast growth on agar media of different density. The final column is the ratio of the standard deviation to the mean cell count for that agar density, which was used in the synthetic data generation.

Agar Density (%)	n	**Mean Cell Count** [cells]	**Standard Deviation** [cells]	**Relative Std. Dev.**
0.6	4	1.06×10^9	9.25×10^7	0.0873
0.8	4	1.40×10^9	1.82×10^8	0.130
1.2	4	1.60×10^9	1.64×10^8	0.103
2.0	3	1.12×10^9	1.38×10^8	0.123

per Table A.1. We then converted the cell count to aspect ratio using the procedure described in the main manuscript, assuming constant $S(t)$.

A.3 Cell Viability

We measured the proportion of living and dead cells in the colony biofilm on Day 14 of growth. Flow cytometry was used to detect Phloxine B stained cells, which we took to indicate dead cells [1, 2]. Collecting this data is invasive, so these experiments were terminated on Day 14 and not included in the data set for the colony biofilm half-width. To avoid terminating more experiments than necessary, we used two experimental replicates to characterise cell viability, one on each of 0.6% and 2.0% agar. A summary of the cell viability experimental data is shown in Figure A.4.

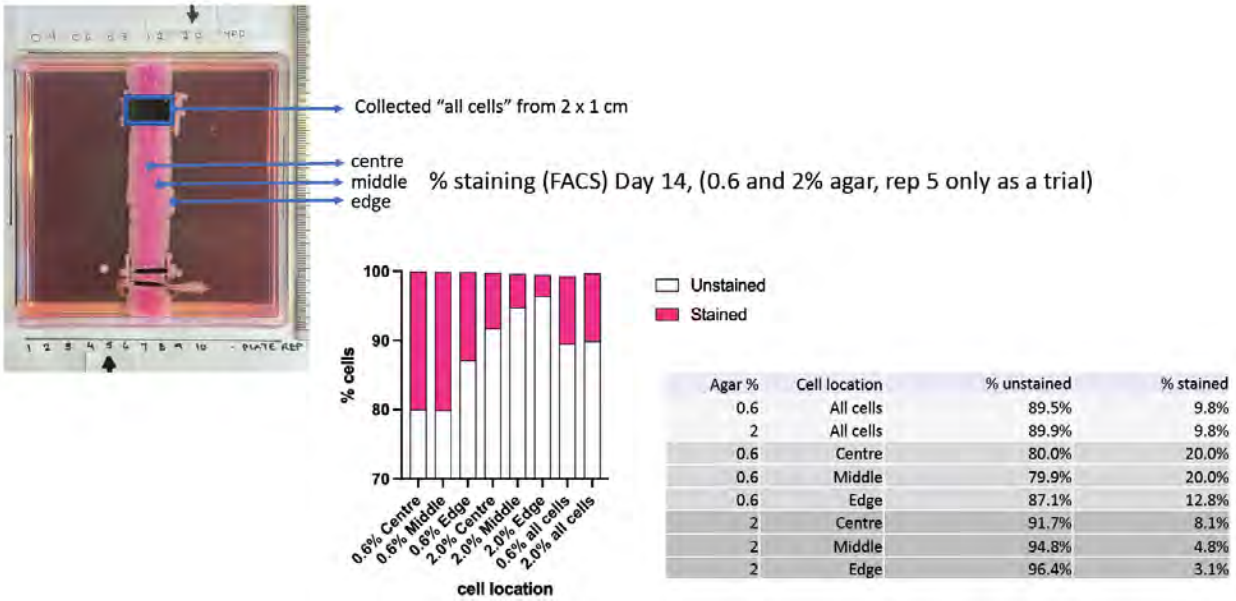

Agar %	Cell location	% unstained	% stained
0.6	All cells	89.5%	9.8%
2	All cells	89.9%	9.8%
0.6	Centre	80.0%	20.0%
0.6	Middle	79.9%	20.0%
0.6	Edge	87.1%	12.8%
2	Centre	91.7%	8.1%
2	Middle	94.8%	4.8%
2	Edge	96.4%	3.1%

Figure A.4: Experimental procedure and results for the cell viability measurements.

As the annotated experimental photograph indicates, the total cell sampling from the blue box provided a larger and more reliable source of cell viability data. The proportions of viable cells were very similar for colonies grown on 0.6% and 2.0% agar. The viability for three spatial locations across the colony biofilm are also provided in Figure A.4. Since these were collected from small samples, there is variability in the results for 0.6% and 2.0% agar. However, on both agar densities the cell viability was lower in the centre than at the edge. We took the mean of the 0.6% and 2.0% data to yield the cell viability data used in the parameter estimation. When generating synthetic data, we scaled the mean cell viability data at each location by the same factor drawn from the uniform distribution $U(0.932, 1.05)$. This ensured that the minimum possible viability in the synthetic data at $x = 0$ is 80%, and that the maximum possible viability at $x = S(t)$ is 96.4%, as per the experimental results in Figure A.4.

B Mathematical Model Derivation

Our mathematical model closely follows Tam [3] and Tam et al. [4], but we present full details here for completeness. We model colony biofilm expansion over an agar substratum, from which the colony biofilm obtains nutrients [3–6]. We formulate the model in 1D Cartesian geometry, as illustrated in Figure B.1.

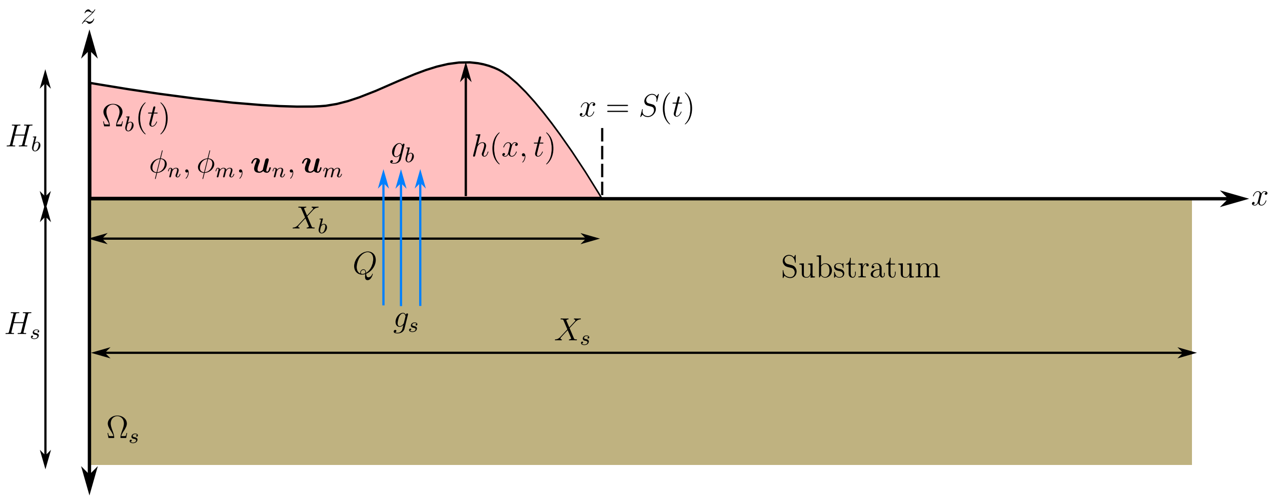

Figure B.1: Schematic of the mathematical model and colony biofilm geometry. See the text for the definition of each symbol.

The colony biofilm exists in the region $\Omega_b(t)$ bounded by $0 < x < S(t)$ and $0 < z < h(x,t)$. The domain Ω_s represents the agar substratum, and is the fixed region bounded by $-H_s < z < 0$, and $0 < x < X_s$ where H_s and X_s are the Petri dish depth and width, respectively. We assume that the colony biofilm consists of two phases, both of which are Newtonian viscous fluids. The phases are an active biomass phase containing proliferating cells and EPS, and an inactive biomass phase consisting of dead cells and extracellular material. We formulate the model using mixture theory, where the volume fractions ϕ_n and ϕ_m satisfy the no-voids condition, $\phi_n + \phi_m = 1$. Since the two phases cannot physically occupy the same space, when introducing the volume fractions we assume that appropriate ensemble averaging has occurred, according to the process outlines by Drew [7]. We assume that the agar substratum cannot deform. The substratum contains nutrients, which we assume occupy no volume. The colony biofilm can take up nutrients through the biofilm–substratum interface. After uptake, nutrients become available for consumption, driving cell proliferation and colony biofilm expansion. Under this two-phase framework, the model variables are

- $h(x, t)$: Colony biofilm height.
- $\phi_n(x, z, t)$: Volume fraction of active biomass (living cells, EPS).
- $\phi_m(x, z, t)$: Volume fraction of inactive biomass (dead cells, water).
- $g_s(x, z, t)$: Nutrient concentration in the substratum, defined in Ω_s.
- $g_b(x, z, t)$: Nutrient concentration in the colony biofilm, defined in $\Omega_b(t)$.
- $\boldsymbol{u}_\alpha(x, y, t) = (u_\alpha(x, y, t), w_\alpha(x, y, t))$: Fluid velocity of phase $\alpha = n, m$.
- $p_\alpha(x, z, t)$: Fluid pressure of phase $\alpha = n, m$.

We also use the symbols X_b and H_b to denote the characteristic width and height of the colony biofilm, respectively.

B.1 Mass Conservation

We obtain governing equations using the principles of mass and momentum conservation. The volume fractions for both phases obey the continuity equation

$$\frac{\partial \rho_\alpha}{\partial t} + \nabla \cdot (\rho_\alpha \boldsymbol{u}_\alpha) = J_\alpha, \tag{B.1}$$

where ρ_α is the density of phase α, and J_α is a source term describing net production of phase α. We assume that both fluid phases are incompressible, such that their densities ρ_α are constant. For the source terms J_α, we assume first order kinetics, whereby cell proliferation is proportional to the local active volume fraction and nutrient concentration, and cell death is proportional to the local active volume fraction. Upon death, cells immediately become part of the inactive phase, with no corresponding change in volume. Under these assumptions, the no-voids and mass conservation equations for the two phases read

$$\phi_n + \phi_m = 1, \tag{B.2a}$$

$$\frac{\partial \phi_n}{\partial t} + \frac{\partial}{\partial x}(\phi_n u_n) + \frac{\partial}{\partial z}(\phi_n w_n) = \psi_n \phi_n g_b - \psi_d \phi_n, \tag{B.2b}$$

$$\frac{\partial \phi_m}{\partial t} + \frac{\partial}{\partial x}(\phi_m u_m) + \frac{\partial}{\partial z}(\phi_m w_m) = \psi_d \phi_n, \tag{B.2c}$$

where ψ_n is the cell proliferation rate and ψ_d is the cell death rate, both of which we assume constant. Adding (B.2b) and (B.2c) and applying the no-voids condition allows us to eliminate ϕ_m to write the system (B.2) in the form

$$\frac{\partial u}{\partial x} + \frac{\partial w}{\partial z} = \psi_n \phi_n g_b, \tag{B.3a}$$

$$\frac{\partial \phi_n}{\partial t} + \frac{\partial}{\partial x}\left(\phi_n u_n\right) + \frac{\partial}{\partial z}\left(\phi_n w_n\right) = \psi_n \phi_n g_b - \psi_d \phi_n, \tag{B.3b}$$

where $\boldsymbol{u} = (u, w) = (\phi_n u_n + \phi_m u_m, \phi_n w_n + \phi_m w_m)$, is the mixture-averaged fluid velocity.

Nutrient disperse by diffusion in the substratum, and by diffusion and advection in the colony biofilm, where they also become available for consumption. Thus, the nutrient concentrations satisfy the equations

$$\frac{\partial g_s}{\partial t} = D_s \left(\frac{\partial^2 g_s}{\partial x^2} + \frac{\partial^2 g_s}{\partial z^2} \right), \tag{B.4a}$$

$$\frac{\partial g_b}{\partial t} + \frac{\partial}{\partial x}\left(g_b u\right) + \frac{\partial}{\partial z}\left(g_b w\right) = D_b \left(\frac{\partial^2 g_b}{\partial x^2} + \frac{\partial^2 g_b}{\partial z^2} \right) - \eta \phi_n g_b, \tag{B.4b}$$

where D_s and D_b are nutrient diffusion coefficients, and η is the maximum nutrient consumption rate.

B.2 Momentum Conservation

We obtain the remaining governing equations using conservation of momentum. Since colony biofilm flows are very viscous, with Re ≈ 0.001 [8], we neglect inertia such that Cauchy's momentum equation applied to one phase becomes

$$\nabla \cdot \left(\phi_\alpha \boldsymbol{\sigma}_\alpha\right) + \boldsymbol{F}_\alpha = \mathbf{0}, \tag{B.5}$$

where $\boldsymbol{\sigma}_\alpha$ is the stress tensor, and $\boldsymbol{F}_\alpha$ represents external sources of momentum. We assume that the entire colony biofilm is a Newtonian viscous material, such that the stress tensor for a given phase is

$$\boldsymbol{\sigma}_\alpha = -\left(p_\alpha + \frac{2\mu_\alpha}{3} \nabla \cdot \boldsymbol{u}_\alpha \right) \boldsymbol{I} + \mu_\alpha \left[\nabla \boldsymbol{u}_\alpha + \left(\nabla \boldsymbol{u}_\alpha\right)^T \right], \tag{B.6}$$

where $\boldsymbol{I}$ is the identity tensor, and μ_α is the dynamic viscosity. Owing to cell proliferation, the velocity field is not necessarily divergence free, so we invoke Stokes' hypothesis [4, 9–11], such that the coefficient of the bulk viscosity (divergence of velocity) term in (B.6) is $-2\mu_\alpha/3$. Due to Newton's third law, the momentum sources are equal and opposite, $\boldsymbol{F}_n = -\boldsymbol{F}_m$. We assume that these momentum sources consist of interphase drag and interfacial forces. Since both phases consist of biological material dispersed within a continuous fluid, we propose interfacial forces of the same form as Lemon et al. [12], as originally derived by Drew and Segel [13]. This yields $\boldsymbol{F}_n = -k(\boldsymbol{u}_n - \boldsymbol{u}_m) + p_n\nabla\phi_n$ and $\boldsymbol{F}_m = -k(\boldsymbol{u}_m - \boldsymbol{u}_n) + p_m\nabla\phi_m$, where $k(\phi_n, \phi_m)$ is the interphase drag coefficient. Componentwise, the momentum balances then contribute two equations per phase (four equations total) to the model,

$$-\frac{\partial p_\alpha}{\partial x} + \mu_\alpha\left(\frac{\partial^2 u_\alpha}{\partial x^2} + \frac{\partial^2 u_\alpha}{\partial z^2}\right) + \frac{\mu_\alpha}{3}\frac{\partial}{\partial x}\left(\frac{\partial u_\alpha}{\partial x} + \frac{\partial w_\alpha}{\partial z}\right) = k(u_\alpha - u_\beta), \tag{B.7a}$$

$$-\frac{\partial p_\alpha}{\partial z} + \mu_\alpha\left(\frac{\partial^2 w_\alpha}{\partial x^2} + \frac{\partial^2 w_\alpha}{\partial z^2}\right) + \frac{\mu_\alpha}{3}\frac{\partial}{\partial z}\left(\frac{\partial u_\alpha}{\partial x} + \frac{\partial w_\alpha}{\partial z}\right) = k(w_\alpha - w_\beta), \tag{B.7b}$$

where the subscript β denotes the opposite phase to α, μ_α is the dynamic viscosity for phase α.

B.3 Initial and Boundary Conditions

When deriving the model we leave the initial conditions general, and write

$$g_s(x, z, 0) = \mathcal{G}(x, z), \tag{B.8a}$$

$$g_b(x, z, 0) = 0, \tag{B.8b}$$

$$\phi_n(x, z, 0) = \Phi(x, z), \tag{B.8c}$$

$$h(x, 0) = \mathcal{H}(x), \tag{B.8d}$$

Precise forms for (B.8) will be determined later, informed by experiments. Several boundary conditions are required to close the model, and we initially consider conditions on horizontal interfaces. For the nutrients, we include conditions on the substratum base, biofilm–substratum interface, and the colony biofilm free surface. Nutrients cannot pass through the base of the substratum, yielding a no-flux condition. In general, the no-flux condition is $\boldsymbol{q} \cdot \hat{\boldsymbol{n}} = 0$, where $\boldsymbol{q}$ is the flux and $\hat{\boldsymbol{n}}$ is the unit outward normal vector to the relevant surface. At the substratum base, the no-flux condition is

$$\frac{\partial g_s}{\partial z} = 0 \quad \text{on} \quad z = -H_s. \tag{B.9}$$

Colony biofilms take up nutrients from the substratum. We assume that nutrient uptake occurs at a rate proportional to the difference in nutrient concentrations across the biofilm–substratum interface. This yields the two conditions

$$D_s \frac{\partial g_s}{\partial z} = -Q\left(g_s - g_b\right) \quad \text{on} \quad z = 0, \tag{B.10a}$$

$$D_b \frac{\partial g_b}{\partial z} = -Q\left(g_s - g_b\right) \quad \text{on} \quad z = 0, \tag{B.10b}$$

where Q is a mass transfer coefficient describing the rate of nutrient uptake. Finally, nutrients in the colony biofilm cannot pass through the free surface. Since the unit outward normal vector to the free surface is $\hat{\boldsymbol{n}} = (-h_x, 1)$, we obtain the no-flux condition

$$g_b\left(u\frac{\partial h}{\partial x} - w\right) = D_b\left(\frac{\partial g_b}{\partial x}\frac{\partial h}{\partial x} - \frac{\partial g_b}{\partial z}\right) \quad \text{on} \quad z = h. \tag{B.11}$$

We obtain the remaining boundary conditions for the colony biofilm from standard conditions from fluid mechanics. On the biofilm–substratum interface, the no penetration condition yields

$$w_\alpha = 0 \quad \text{on} \quad z = 0. \tag{B.12}$$

The tangential stress condition on the biofilm–substratum interface reads $\hat{\boldsymbol{t}} \cdot (\phi_\alpha \boldsymbol{\sigma}_\alpha \cdot \hat{\boldsymbol{n}}) = \lambda_\alpha(\phi_\alpha \boldsymbol{u}_\alpha \cdot \hat{\boldsymbol{t}})$, where $\hat{\boldsymbol{t}}$ is any unit tangent vector, and the new constant λ_α is a slip coefficient representing the adhesion strength between the fluid phase and the agar. This yields the slip boundary condition

$$\mu_\alpha\left(\frac{\partial u_\alpha}{\partial z} + \frac{\partial w_\alpha}{\partial x}\right) = \mu_\alpha \frac{\partial u_\alpha}{\partial z} = \lambda_\alpha u_\alpha \quad \text{on} \quad z = 0, \tag{B.13}$$

Perfect slip corresponds to $\lambda_\alpha = 0$, whereas no slip requires $\lambda_\alpha \to \infty$. On the colony biofilm free surface, the kinematic condition

$$\frac{\partial h}{\partial t} + u_\alpha \frac{\partial h}{\partial x} = w_\alpha \quad \text{on} \quad z = h, \tag{B.14}$$

states that fluid particles initially on the free surface must remain there. We also have one condition per phase stating that the tangential stress is zero on the free surface. That is, $\hat{\boldsymbol{t}} \cdot (\phi_\alpha \boldsymbol{\sigma}_\alpha \cdot \hat{\boldsymbol{n}}) = 0$. In expanded form this condition reads

$$-2\frac{\partial h}{\partial x}\left(\frac{\partial u_\alpha}{\partial x} - \frac{\partial w_\alpha}{\partial z}\right) + \frac{\partial u_\alpha}{\partial z} + \frac{\partial w_\alpha}{\partial x} - \left(\frac{\partial h}{\partial x}\right)^2\left(\frac{\partial u_\alpha}{\partial z} + \frac{\partial w_\alpha}{\partial x}\right) = 0 \quad \text{on} \quad z = h. \tag{B.15}$$

Finally, we impose zero normal stress on the free surface, $\hat{\boldsymbol{n}} \cdot (\phi_\alpha \boldsymbol{\sigma}_\alpha \cdot \hat{\boldsymbol{n}}) = 0$. This boundary condition assumes zero surface tension. Surface tension might represent the typical fluid surface tension, or the strength of cell–cell adhesion at the biofilm–air interface [14]. For colony biofilms expanding by sliding motility [15, 16], cell–cell adhesion forces are weak. Previously, we showed that surface tension has minimal impact on the colony biofilm expansion speed [4]. Surface tension primarily impacted colony biofilm shape by mitigating ridge formation, an effect that is unimportant to the experimental results in this manuscript. Therefore, we neglect surface tension in the model. The normal stress condition on the free surface is then

$$\begin{aligned} p_\alpha + \frac{2\mu_\alpha}{3}\left(\frac{\partial u_\alpha}{\partial x} + \frac{\partial w_\alpha}{\partial z}\right) \\ = \mu_\alpha\left[2\left(\frac{\partial h}{\partial x}\right)^2\frac{\partial u_\alpha}{\partial x} + 2\frac{\partial w_\alpha}{\partial z} - \frac{\partial h}{\partial x}\left(\frac{\partial u_\alpha}{\partial z} + \frac{\partial w_\alpha}{\partial x}\right)\right]\left[1 + \left(\frac{\partial h}{\partial x}\right)^2\right]^{-3/2} \quad \text{on} \quad z = h. \end{aligned} \tag{B.16}$$

Equations (B.2), (B.4) and (B.7), combined with initial conditions (B.8) and boundary conditions (B.9)–(B.16), then form the closed model.

B.4 Model Simplification

When applying mixture theory models to colony biofilm growth, several simplifying assumptions are available, and we apply them prior to nondimensionalisation. O'Dea, Waters, and Byrne [17] built on several studies to show [18, 19] that the interphase drag coefficient is large for flow in a bioreactor. Since the length scales of colony biofilm growth are similar to a bioreactor [17], the same large drag assumption applies. Taking $k \to \infty$ requires $\boldsymbol{u}_n = \boldsymbol{u}_m$ for the momentum source terms to remain bounded. Therefore, one simplification is that both phases move at the common mixture velocity $\boldsymbol{u} = \boldsymbol{u}_n = \boldsymbol{u}_m$. Furthermore, although the precise composition of the colony biofilm is complex, the active and passive biomass phases consist of water, extracellular polymeric substances (EPS), and cellular material. Therefore, we can assume that both phases have common density and viscosity, $\rho_n = \rho_m$ and $\mu_n = \mu_m$. The strength of biofilm–substratum adhesion may depend on the agar density, but can also be assumed the same across the two phases, $\lambda = \lambda_n = \lambda_m$. Owing to the similarity of other physical properties, the pressure, $p = p_n = p_m$, is also assumed the same for both phases. Under these assumptions, the model reduces to (where all PDEs apply in $\Omega_b(t)$, except the equation for g_s which applies in Ω_s)

$$\frac{\partial u}{\partial x} + \frac{\partial w}{\partial z} = \psi_n \phi_n g_b, \tag{B.17a}$$

$$\frac{\partial \phi_n}{\partial t} + \frac{\partial}{\partial x}(\phi_n u) + \frac{\partial}{\partial z}(\phi_n w) = \psi_n \phi_n g_b - \psi_d \phi_n, \tag{B.17b}$$

$$\frac{\partial g_s}{\partial t} = D_s \left(\frac{\partial^2 g_s}{\partial x^2} + \frac{\partial^2 g_s}{\partial z^2} \right), \tag{B.17c}$$

$$\frac{\partial g_b}{\partial t} + \frac{\partial}{\partial x}(g_b u) + \frac{\partial}{\partial z}(g_b w) = D_b \left(\frac{\partial^2 g_b}{\partial x^2} + \frac{\partial^2 g_b}{\partial z^2} \right) - \eta \phi_n g_b, \tag{B.17d}$$

$$-\frac{\partial p}{\partial x} + \mu \left(\frac{\partial^2 u}{\partial x^2} + \frac{\partial^2 u}{\partial z^2} \right) + \frac{\mu}{3} \frac{\partial}{\partial x} \left(\frac{\partial u}{\partial x} + \frac{\partial w}{\partial z} \right) = 0, \tag{B.17e}$$

$$-\frac{\partial p}{\partial z} + \mu \left(\frac{\partial^2 w}{\partial x^2} + \frac{\partial^2 w}{\partial z^2} \right) + \frac{\mu}{3} \frac{\partial}{\partial z} \left(\frac{\partial u}{\partial x} + \frac{\partial w}{\partial z} \right) = 0, \tag{B.17f}$$

and is subject to the initial conditions (B.8) and boundary conditions

$$\frac{\partial g_s}{\partial z} = 0 \quad \text{on} \quad z = -H_s, \tag{B.18a}$$

$$D_s \frac{\partial g_s}{\partial z} = -Q\left(g_s - g_b\right) \quad \text{on} \quad z = 0, \tag{B.18b}$$

$$D_b \frac{\partial g_b}{\partial z} = -Q\left(g_s - g_b\right) \quad \text{on} \quad z = 0, \tag{B.18c}$$

$$w = 0 \quad \text{on} \quad z = 0, \tag{B.18d}$$

$$\mu \frac{\partial u}{\partial z} = \lambda u \quad \text{on} \quad z = 0, \tag{B.18e}$$

$$g_b\left(u\frac{\partial h}{\partial x} - w\right) = D_b\left(\frac{\partial g_b}{\partial x}\frac{\partial h}{\partial x} - \frac{\partial g_b}{\partial z}\right) \quad \text{on} \quad z = h, \tag{B.18f}$$

$$\frac{\partial h}{\partial t} + u\frac{\partial h}{\partial x} = w \quad \text{on} \quad z = h, \tag{B.18g}$$

$$-2\frac{\partial h}{\partial x}\left(\frac{\partial u}{\partial x} - \frac{\partial w}{\partial z}\right) + \frac{\partial u}{\partial z} + \frac{\partial w}{\partial x} - \left(\frac{\partial h}{\partial x}\right)^2\left(\frac{\partial u}{\partial z} + \frac{\partial w}{\partial x}\right) = 0 \quad \text{on} \quad z = h, \tag{B.18h}$$

$$\begin{aligned} &p + \frac{2\mu}{3}\left(\frac{\partial u}{\partial x} + \frac{\partial w}{\partial z}\right) \\ &= \mu\left[2\left(\frac{\partial h}{\partial x}\right)^2\frac{\partial u}{\partial x} + 2\frac{\partial w}{\partial z} - \frac{\partial h}{\partial x}\left(\frac{\partial u}{\partial z} + \frac{\partial w}{\partial x}\right)\right]\left[1 + \left(\frac{\partial h}{\partial x}\right)^2\right]^{-3/2} \quad \text{on} \quad z = h. \end{aligned} \tag{B.18i}$$

B.5 Nondimensionalisation

We nondimensionalise by introducing dimensionless variables denoted with carets, and the scalings

$$\begin{gathered} t = \frac{X_b^2}{D_b}\hat{t}, \quad (x, z) = \left(X_b\hat{x}, \varepsilon X_b\hat{z}\right), \quad (u, w) = \left(\frac{D_b}{X_b}\hat{u}, \frac{\varepsilon D_b}{X_b}\hat{w}\right), \\ g_s = G\hat{g}_s, \quad g_b = G\hat{g}_b, \quad \text{and} \quad p = \frac{\mu D_b}{X_b^2}\hat{p}, \end{gathered} \tag{B.19}$$

where $X_b = S(0)$ is the initial colony biofilm size, and $\varepsilon = H_b/X_b = H_s/X_s \ll 1$ is a small (thin-film) parameter. Previously, in Tam et al. [4] we assumed that the substratum and colony biofilm were of similar size. To accurately compare the model with experiments, we need to account for the difference in length scales in the colony biofilm and substratum, which we achieve by defining the parameter $\delta = X_b/X_s$. The dimensionless governing equations are then (where all PDEs apply in $\Omega_b(t)$, except the equation for g_s which applies in Ω_s)

$$\frac{\partial u}{\partial x}+\frac{\partial w}{\partial z}=\Psi_n\phi_n g_b, \tag{B.20a}$$

$$\frac{\partial \phi_n}{\partial t}+\frac{\partial}{\partial x}\left(\phi_n u\right)+\frac{\partial}{\partial z}\left(\phi_n w\right)=\Psi_n\phi_n g_b-\Psi_d\phi_n, \tag{B.20b}$$

$$\frac{\partial g_s}{\partial t}=D\left(\frac{\partial^2 g_s}{\partial x^2}+\frac{1}{\varepsilon^2}\frac{\partial^2 g_s}{\partial z^2}\right), \tag{B.20c}$$

$$\frac{\partial g_b}{\partial t}+\frac{\partial}{\partial x}\left(g_b u\right)+\frac{\partial}{\partial z}\left(g_b w\right)=\frac{\partial^2 g_b}{\partial x^2}+\frac{1}{\varepsilon^2}\frac{\partial^2 g_b}{\partial z^2}-\Upsilon\phi_n g_b, \tag{B.20d}$$

$$-\frac{\partial p}{\partial x}+\frac{\partial^2 u}{\partial x^2}+\frac{1}{\varepsilon^2}\frac{\partial^2 u}{\partial z^2}+\frac{1}{3}\frac{\partial}{\partial x}\left(\frac{\partial u}{\partial x}+\frac{\partial w}{\partial z}\right)=0, \tag{B.20e}$$

$$-\frac{\partial p}{\partial z}+\varepsilon^2\frac{\partial^2 w}{\partial x^2}+\frac{\partial^2 w}{\partial z^2}+\frac{1}{3}\frac{\partial}{\partial z}\left(\frac{\partial u}{\partial x}+\frac{\partial w}{\partial z}\right)=0, \tag{B.20f}$$

subject to the boundary conditions,

$$\frac{\partial g_s}{\partial z}=0 \quad \text{on} \quad z=-1/\delta, \tag{B.21a}$$

$$\frac{\partial g_s}{\partial z}=-\varepsilon^2\frac{Q^*}{D}\left(g_s-g_b\right) \quad \text{on} \quad z=0, \tag{B.21b}$$

$$\frac{\partial g_b}{\partial z}=-\varepsilon^2 Q^*\left(g_s-g_b\right) \quad \text{on} \quad z=0, \tag{B.21c}$$

$$w=0 \quad \text{on} \quad z=0, \tag{B.21d}$$

$$\frac{\partial u}{\partial z}=\varepsilon^2\lambda^* u \quad \text{on} \quad z=0, \tag{B.21e}$$

$$g_b\left(u\frac{\partial h}{\partial x}-w\right)=\frac{\partial g_b}{\partial x}\frac{\partial h}{\partial x}-\frac{1}{\varepsilon^2}\frac{\partial g_b}{\partial z} \quad \text{on} \quad z=h, \tag{B.21f}$$

$$\frac{\partial h}{\partial t}+u\frac{\partial h}{\partial x}=w \quad \text{on} \quad z=h, \tag{B.21g}$$

$$-2\frac{\partial h}{\partial x}\left(\frac{\partial u}{\partial x}-\frac{\partial w}{\partial z}\right)+\frac{1}{\varepsilon^2}\frac{\partial u}{\partial z}+\frac{\partial w}{\partial x}-\left(\frac{\partial h}{\partial x}\right)^2\left(\frac{\partial u}{\partial z}+\varepsilon^2\frac{\partial w}{\partial x}\right)=0 \quad \text{on} \quad z=h, \tag{B.21h}$$

$$\begin{aligned} p+\frac{2}{3}\left(\frac{\partial u}{\partial x}+\frac{\partial w}{\partial z}\right)=&\left[2\varepsilon^2\left(\frac{\partial h}{\partial x}\right)^2\frac{\partial u}{\partial x}+2\frac{\partial w}{\partial z}\right.\\ &\left.-\frac{\partial h}{\partial x}\left(\frac{\partial u}{\partial z}+\varepsilon^2\frac{\partial w}{\partial x}\right)\right]\left[1+\varepsilon^2\left(\frac{\partial h}{\partial x}\right)^2\right]^{-3/2} \end{aligned} \quad \text{on} \quad z=h. \tag{B.21i}$$

In writing (B.20) and (B.21), we have introduced the dimensionless parameters

$$\begin{gathered} \Psi_n=\frac{GX_b^2\psi_n}{D_b}, \quad \Psi_d=\frac{X_b^2\psi_d}{D_b}, \quad D=\frac{D_s}{D_b}, \\ \Upsilon=\frac{X_b^2\eta}{D_b}, \quad Q^*=\frac{X_bQ}{\varepsilon D_b}, \quad \text{and} \quad \lambda^*=\frac{X_b\lambda}{\varepsilon\mu}. \end{gathered} \tag{B.22}$$

B.6 Thin-Film Approximation

We now apply the thin-film (long-wave) approximation to obtain a leading order in ε model. Expanding variables in power series of ε^2,

$$h(x,y,t) \sim h_0(x,y,t) + \varepsilon^2 h_1(x,y,t) + \mathcal{O}(\varepsilon^4), \tag{B.23}$$

and so on, where the expansions for the other variables take the same form as (B.23). The leading order governing equations are then

$$\begin{aligned}
\frac{\partial u_0}{\partial x} + \frac{\partial w_0}{\partial z} &= \Psi_n \phi_{n0} g_{b0}, && \text{(B.24a)}\\
\frac{\partial \phi_{n0}}{\partial t} + \frac{\partial}{\partial x}(\phi_{n0} u_0) + \frac{\partial}{\partial z}(\phi_{n0} w_0) &= \Psi_n \phi_{n0} g_{b0} - \Psi_d \phi_{n0}, && \text{(B.24b)}\\
\frac{\partial^2 g_{s0}}{\partial z^2} &= 0, && \text{(B.24c)}\\
\frac{\partial^2 g_{b0}}{\partial z^2} &= 0, && \text{(B.24d)}\\
\frac{\partial^2 u_0}{\partial z^2} &= 0, && \text{(B.24e)}\\
-\frac{\partial p_0}{\partial z} + \frac{\partial^2 w_0}{\partial z^2} + \frac{1}{3}\frac{\partial}{\partial z}\left(\frac{\partial u_0}{\partial x} + \frac{\partial w_0}{\partial z}\right) &= 0, && \text{(B.24f)}
\end{aligned}$$

and the leading order boundary conditions become

$$\begin{aligned}
\frac{\partial g_{s0}}{\partial z} &= 0 && \text{on} \quad z = -1/\delta, 0, && \text{(B.25a)}\\
\frac{\partial g_{b0}}{\partial z} &= 0 && \text{on} \quad z = 0, h_0, && \text{(B.25b)}\\
\frac{\partial u_0}{\partial z} &= 0 && \text{on} \quad z = 0, h_0, && \text{(B.25c)}\\
w_0 &= 0 && \text{on} \quad z = 0, && \text{(B.25d)}\\
w_0 &= \frac{\partial h_0}{\partial t} + u_0 \frac{\partial h_0}{\partial x} && \text{on} \quad z = h_0, && \text{(B.25e)}\\
-p_0 - \frac{2}{3}\frac{\partial u_0}{\partial x} + \frac{4}{3}\frac{\partial w_0}{\partial z} &= 0 && \text{on} \quad z = h_0. && \text{(B.25f)}
\end{aligned}$$

As expected for an extensional flow, the systems (B.24) and (B.25) indicate that the leading order nutrient concentrations g_{s0} and g_{b0}, and the leading order horizontal velocity u_0 do not depend on z. To proceed, we also define the depth-averaged cell volume fraction

$$\bar{\phi}_0(x,t) = \frac{1}{h_0}\int_0^{h_0} \phi_{n0}(x,z,t)\,\mathrm{d}z. \tag{B.26}$$

On defining (B.26), we exploit the z-independence and integrate the mass balance equations (B.24a) and (B.24b) with respect to z from 0 to h_0, yielding

$$\frac{\partial h_0}{\partial t} + \frac{\partial}{\partial x}\left(u_0 h_0\right) = \Psi_n \bar{\phi}_0 g_{b0} h_0, \tag{B.27a}$$

$$\frac{\partial}{\partial t}\left(\bar{\phi}_0 h_0\right) + \frac{\partial}{\partial x}\left(\bar{\phi}_0 u_0 h_0\right) = \Psi_n \bar{\phi}_0 g_{b0} h_0 - \Psi_d \bar{\phi}_0 h_0, \tag{B.27b}$$

where we have applied Leibniz's integral rule in obtaining (B.27b).

Since the leading order equations for g_{s0}, g_{b0}, and u_0 yielded z-independence, to obtain governing equations for these variables we consider the higher order correction terms. Using the dimensionless model and thin-film expansions (B.20), (B.21) and (B.23), the relevant equations at $\mathcal{O}(\varepsilon^2)$ are

$$\frac{\partial^2 g_{s1}}{\partial z^2} = \frac{1}{D}\frac{\partial g_{s0}}{\partial t} - \frac{\partial^2 g_{s0}}{\partial x^2}, \tag{B.28a}$$

$$\frac{\partial^2 g_{b1}}{\partial z^2} = \frac{\partial g_{b0}}{\partial t} + \frac{\partial}{\partial x}\left(g_{b0}u_0\right) + \frac{\partial}{\partial z}\left(g_{b0}w_0\right) - \frac{\partial^2 g_{b0}}{\partial x^2} + \Upsilon \phi_{n0} g_{b0}, \tag{B.28b}$$

$$\frac{\partial^2 u_1}{\partial z^2} = \frac{\partial p_0}{\partial x} - \frac{\partial^2 u_0}{\partial x^2} - \frac{1}{3}\frac{\partial}{\partial x}\left(\frac{\partial u_0}{\partial x} + \frac{\partial w_0}{\partial z}\right), \tag{B.28c}$$

with boundary conditions

$$\frac{\partial g_{s1}}{\partial z} = 0 \qquad \text{on} \quad z = -1/\delta, \tag{B.29a}$$

$$\frac{\partial g_{s1}}{\partial z} = -\frac{Q^*}{D}\left(g_{s0} - g_{b0}\right) \qquad \text{on} \quad z = 0, \tag{B.29b}$$

$$\frac{\partial g_{b1}}{\partial z} = -Q^*\left(g_{s0} - g_{b0}\right) \qquad \text{on} \quad z = 0, \tag{B.29c}$$

$$\frac{\partial g_{b1}}{\partial z} = \frac{\partial g_{b0}}{\partial x}\frac{\partial h_0}{\partial x} - g_{b0}\left(u_0\frac{\partial h_0}{\partial x} - w_0\right) \qquad \text{on} \quad z = h_0, \tag{B.29d}$$

$$\frac{\partial u_1}{\partial z} = \lambda^* u_0 \qquad \text{on} \quad z = 0, \tag{B.29e}$$

$$\frac{\partial u_1}{\partial z} = 2\frac{\partial h_0}{\partial x}\left(\frac{\partial u_0}{\partial x} - \frac{\partial w_0}{\partial z}\right) - \frac{\partial w_0}{\partial x} \qquad \text{on} \quad z = h_0. \tag{B.29f}$$

Integrating the correction terms for the nutrient concentration (B.28a) and (B.28b) with respect to z and applying the boundary conditions (B.29a)–(B.29d) yields equations for the leading order nutrient concentrations,

$$\frac{\partial g_{s0}}{\partial t} = D\frac{\partial^2 g_{s0}}{\partial x^2} - \delta Q^* \left(g_{s0} - g_{b0}\right), \tag{B.30a}$$

$$h_0\frac{\partial g_{b0}}{\partial t} + \frac{\partial}{\partial x}\left(u_0 h_0 g_{b0}\right) = \frac{\partial}{\partial x}\left(h_0\frac{\partial g_{b0}}{\partial x}\right) + Q^*\left(g_{s0} - g_{b0}\right) - \Upsilon\bar{\phi}_0 g_{b0} h_0. \tag{B.30b}$$

A similar depth-integration procedure yields an equation for the leading order horizontal velocity, u_0. First, we rewrite the correction for the x-component of momentum (B.28c) using the mass balance (B.24a) to obtain

$$\frac{\partial^2 u_1}{\partial z^2} = \frac{\partial p_0}{\partial x} - 2\frac{\partial^2 u_0}{\partial x^2} - \frac{\partial^2 w_0}{\partial x\,\partial z} + \frac{2\Psi_n}{3}\frac{\partial}{\partial x}\left(\phi_{n0} g_{b0}\right). \tag{B.31}$$

Integrating the correction term for the horizontal velocity (B.31) once with respect to z and applying the boundary conditions (B.29e) and (B.29f) yields, on application of Leibniz's integral rule for pressure and volume fraction terms,

$$\begin{aligned} 2\frac{\partial h_0}{\partial x}\left(\frac{\partial u_0}{\partial x} - \left.\frac{\partial w_0}{\partial z}\right|_{z=h_0}\right) - \left.\frac{\partial w_0}{\partial x}\right|_{z=h_0} - \lambda^* u_0 &= \frac{\partial}{\partial x}\left(\int_0^{h_0} p_0\,\mathrm{d}z\right) - p_0(h_0)\frac{\partial h_0}{\partial x} \\ -2h_0\frac{\partial^2 u_0}{\partial x^2} - \left[\frac{\partial w_0}{\partial x}\right]_0^{h_0} &+ \frac{2\Psi_n}{3}\frac{\partial}{\partial x}\left(\int_0^{h_0}\phi_{n0} g_{b0}\,\mathrm{d}z\right) - \frac{2\Psi_n}{3}\phi_{n0}(h_0) g_{b0}\frac{\partial h_0}{\partial x}. \end{aligned} \tag{B.32}$$

Derivatives of w_0 with respect to x cancel. To solve for the leading order pressure p_0, we integrate (B.24f) to obtain

$$p_0 = \frac{4}{3}\frac{\partial w_0}{\partial z} + \frac{1}{3}\frac{\partial u_0}{\partial x} + C(x). \tag{B.33}$$

Applying the boundary condition (B.25f) for the leading-order pressure on $z = h_0$ determines the constant of integration

$$C(x) = -\frac{\partial u_0}{\partial x} \implies p_0 = -\frac{4}{3}\frac{\partial w_0}{\partial z} - \frac{2}{3}\frac{\partial u_0}{\partial x} = -2\frac{\partial u_0}{\partial x} + \frac{4\Psi_n}{3}\phi_{n0} g_{b0} = 2\frac{\partial w_0}{\partial z} - \frac{2\Psi_n}{3}\phi_{n0} g_{b0}, \tag{B.34}$$

where we have used the mass balance (B.24a) to obtain two alternative forms for p_0. Substituting the expression for pressure (B.34) into the integrated $\mathcal{O}(\varepsilon^2)$ momentum equation (B.32) then yields

$$
\begin{aligned}
2\frac{\partial h_0}{\partial x}\left(\frac{\partial u_0}{\partial x}-\left.\frac{\partial w_0}{\partial z}\right|_{z=h_0}\right)-\lambda^* u_0 = {} & \frac{\partial}{\partial x}\left(\int_0^{h_0}\frac{4\Psi_n}{3}\phi_{n0}g_{b0}-2\frac{\partial u_0}{\partial x}\,\mathrm{d}z\right) \\
& -\frac{\partial h_0}{\partial x}\left[2\left.\frac{\partial w_0}{\partial z}\right|_{z=h_0}-\frac{2\Psi_n}{3}\phi_{n0}(h_0)g_{b0}\right] \\
& -2h_0\frac{\partial^2 u_0}{\partial x^2}+\frac{2\Psi_n}{3}\frac{\partial}{\partial x}\left(\int_0^{h_0}\phi_{n0}g_{b0}\,\mathrm{d}z\right)-\frac{2\Psi_n}{3}\phi_{n0}(h_0)g_{b0}\frac{\partial h_0}{\partial x}.
\end{aligned}
\tag{B.35}
$$

After evaluating the integrals and simplification, we arrive at the leading order governing equation

$$
4\frac{\partial}{\partial x}\left(h_0\frac{\partial u_0}{\partial x}\right)-\lambda^* u_0 = 2\Psi_n\frac{\partial}{\partial x}\left(\bar{\phi}_0 g_{b0}h_0\right). \tag{B.36}
$$

Equations (B.27), (B.30) and (B.36) then constitute a system of five spatially one-dimensional PDEs for the leading order quantities h_0, $\bar{\phi}_0$, g_{s0}, g_{b0}, and u_0. Recall that Equations (B.36), (B.27a), (B.27b) and (B.30b) are defined within the colony biofilm $x < S(t)$. The nutrient concentration in the substratum (B.30a) is defined for the Petri dish, $0 < x < 1/\delta$. Since nutrient depletion from the substratum can only occur in regions occupied by the colony biofilm, we modify (B.30a) to write

$$
\frac{\partial g_{s0}}{\partial t} = D\frac{\partial^2 g_{s0}}{\partial x^2}-\delta Q^*\left(g_{s0}-g_{b0}\right)H(S(t)-x) \quad \text{on} \quad 0 < x < 1/\delta, \tag{B.37}
$$

where $H(\cdot)$ is the Heaviside step function.

It remains to specify the initial and boundary conditions for PDEs (B.27), (B.36), (B.37) and (B.30b). The initial conditions are

$$g_{s0}(x,0) = 1, \tag{B.38a}$$

$$g_{b0}(x,0) = 0, \tag{B.38b}$$

$$\bar{\phi}_0(x,0) = 0, \tag{B.38c}$$

$$h_0(x,0) = H_0\left(1-x^2\right), \tag{B.38d}$$

$$S(0) = 1. \tag{B.38e}$$

These conditions reflect that there is initially no nutrient or dead cells in the colony biofilm. The substratum nutrient concentration g_{s0} and contact line position S are initially unity because nutrients are scaled by the initial nutrient concentration, and x is scaled by the initial colony biofilm width. Since the initial cell density in experiments is several orders of magnitude less than the cell density of a mature colony biofilm [20], we expect H_0 to be small, even with the thin-film approximation applied.

The boundary conditions for the spatially one-dimensional model consist of no-flux conditions for the nutrients, which become

$$\frac{\partial g_{s0}}{\partial x} = 0 \quad \text{on} \quad x = 0, 1/\delta, \quad \text{and} \quad \frac{\partial g_{b0}}{\partial x} = 0 \quad \text{on} \quad x = 0. \tag{B.39}$$

We also apply the following symmetry conditions at $x = 0$:

$$\frac{\partial h_0}{\partial x} = 0, \quad \frac{\partial \bar{\phi}_0}{\partial x} = 0, \quad u_0 = 0 \quad \text{on} \quad x = 0. \tag{B.40}$$

We obtain the second boundary conditions for g_{b0} using the same argument as Tam et al. [4], yielding

$$\frac{\partial g_{b0}}{\partial x} = 0 \quad \text{on} \quad x = S(t). \tag{B.41}$$

The boundary condition for u_0 comes from imposing zero normal stress, σ_{xx}, at the contact line $x = S(t)$. Using $\sigma_{xx} = -p - 2\mu(u_x + w_z)/3 + 2\mu u_x$, we arrive at the condition

$$\frac{\partial u_0}{\partial x} = \frac{1}{2}\Psi_n \bar{\phi}_0 g_{b0} \quad \text{on} \quad x = S(t). \tag{B.42}$$

B.7 Summary

The complete thin-film, extensional flow model addressed in this work then consists of the differential equations (dropping the zero subscript on leading-order quantities and the overbar on averaged quantities)

$$\frac{\partial h}{\partial t} + \frac{\partial}{\partial x}\left(uh\right) = \Psi_n \phi g_b h \qquad \text{on} \quad 0 < x < S(t), \tag{B.43a}$$

$$\frac{\partial}{\partial t}\left(\phi h\right) + \frac{\partial}{\partial x}\left(\phi u h\right) = \Psi_n \phi g_b h - \Psi_d \phi h \qquad \text{on} \quad 0 < x < S(t), \tag{B.43b}$$

$$\frac{\partial g_s}{\partial t} = D\frac{\partial^2 g_s}{\partial x^2} - \delta Q^* \left(g_s - g_b\right) H(S(t) - x) \qquad \text{on} \quad 0 < x < 1/\delta, \tag{B.43c}$$

$$h\frac{\partial g_b}{\partial t} + \frac{\partial}{\partial x}\left(uhg_b\right) = \frac{\partial}{\partial x}\left(h\frac{\partial g_b}{\partial x}\right) + Q^* \left(g_s - g_b\right) - \Upsilon \phi g_b h \qquad \text{on} \quad 0 < x < S(t), \tag{B.43d}$$

$$4\frac{\partial}{\partial x}\left(h\frac{\partial u}{\partial x}\right) - \lambda^* u = 2\Psi_n \frac{\partial}{\partial x}\left(\phi g_b h\right) \qquad \text{on} \quad 0 < x < S(t), \tag{B.43e}$$

$$\frac{\mathrm{d}S}{\mathrm{d}t} = u(S(t), t), \tag{B.43f}$$

initial conditions

$$g_s(x, 0) = 1, \tag{B.44a}$$

$$g_b(x, 0) = 0, \tag{B.44b}$$

$$\phi(x, 0) = 0, \tag{B.44c}$$

$$h(x, 0) = H_0\left(1 - x^2\right), \tag{B.44d}$$

$$S(0) = 1, \tag{B.44e}$$

and boundary conditions

$$\frac{\partial h}{\partial x} = 0 \qquad \text{on} \quad x = 0, \tag{B.45a}$$

$$\frac{\partial \phi}{\partial x} = 0, \qquad \text{on} \quad x = 0, \tag{B.45b}$$

$$\frac{\partial g_s}{\partial x} = 0 \qquad \text{on} \quad x = 0, 1/\delta, \tag{B.45c}$$

$$\frac{\partial g_b}{\partial x} = 0 \qquad \text{on} \quad x = 0, S(t), \tag{B.45d}$$

$$u = 0 \qquad \text{on} \quad x = 0, \tag{B.45e}$$

$$\frac{\partial u}{\partial x} = \frac{1}{2}\Psi_n \phi g_b \qquad \text{on} \quad x = S(t). \tag{B.45f}$$

An alternative form of the active phase mass balance equation is available by expanding (B.43b) using the product rule and using (B.43a) to obtain

$$\frac{\partial \phi}{\partial t} + u\frac{\partial \phi}{\partial x} = \phi\left[\Psi_n g_b\left(1-\phi\right) - \Psi_d\right] \qquad \text{on} \qquad 0 < x < S(t). \tag{B.46}$$

The form (B.46) is useful for the numerical method, which we now outline.

C Numerical Methods

To solve the model numerically, we map the moving-boundary problem on $0 < x < S(t)$ to the unit interval using the change of variables

$$(\xi, \tau) = \left(\frac{x}{S(t)}, t\right) \implies \frac{\partial}{\partial x} = \frac{1}{S(\tau)} \frac{\partial}{\partial \xi}, \quad \frac{\partial}{\partial t} = \frac{\partial}{\partial \tau} - \frac{\xi S'(\tau)}{S(\tau)} \frac{\partial}{\partial \xi}. \tag{C.1}$$

To circumvent the Heaviside step function, we write Eqn. (B.43c) for the substratum nutrient concentration in piecewise form, and use the symbol g_o, defined for $S(t) < x < 1/\delta$, to denote the nutrient concentration in the region of the Petri dish unoccupied by the colony biofilm. Consequently, g_s is then the nutrient concentration in the substratum, restricted to $0 < x < S(t)$. In distinguishing between g_s and g_o, we also impose that the nutrient concentration in the agar defined over the entire Petri dish is a C^1 function, such that $g_s(S(t), t) = g_o(S(t), t)$ and $g_s'(S(t), t) = g_o'(S(t), t)$. The transformed model in terms of the new independent variables ξ and τ to solve numerically is then

$$\frac{\partial h}{\partial \tau} - \frac{\xi u(1,\tau)}{S} \frac{\partial h}{\partial \xi} + \frac{1}{S} \frac{\partial}{\partial \xi}(uh) = \Psi_n \phi g_b h, \tag{C.2a}$$

$$\frac{\partial \phi}{\partial \tau} + \left[\frac{u - \xi u(1,\tau)}{S}\right] \frac{\partial \phi}{\partial \xi} = \phi \left[\Psi_n g_b (1 - \phi) - \Psi_d\right], \tag{C.2b}$$

$$\frac{\partial g_s}{\partial \tau} - \frac{\xi u(1,\tau)}{S} \frac{\partial g_s}{\partial \xi} = \frac{D}{S^2} \frac{\partial^2 g_s}{\partial \xi^2} - \delta Q^* (g_s - g_b), \tag{C.2c}$$

$$\frac{\partial g_o}{\partial \tau} - \frac{\xi u(1,\tau)}{S} \frac{\partial g_o}{\partial \xi} = \frac{D}{S^2} \frac{\partial^2 g_o}{\partial \xi^2}, \tag{C.2d}$$

$$h \frac{\partial g_b}{\partial \tau} - \frac{\xi u(1,\tau) h}{S} \frac{\partial g_b}{\partial \xi} + \frac{1}{S} \frac{\partial}{\partial \xi}(uhg_b) = \frac{1}{S^2} \frac{\partial}{\partial \xi}\left(h \frac{\partial g_b}{\partial \xi}\right) + Q^* (g_s - g_b) - \Upsilon \phi g_b h, \tag{C.2e}$$

$$\frac{4}{S^2} \frac{\partial}{\partial \xi}\left(h \frac{\partial u}{\partial \xi}\right) - \lambda^* u = \frac{2\Psi_n}{S} \frac{\partial}{\partial \xi}(\phi g_b h), \tag{C.2f}$$

$$\frac{\mathrm{d}S}{\mathrm{d}\tau} = u(1,\tau). \tag{C.2g}$$

All PDEs are solved for $0 \leq \tau \leq T$, such that the PDEs (C.2a)–(C.2c), (C.2e) and (C.2f) are defined for $0 < \xi < 1$ and (C.2d) applies for $1 < \xi < 1/\delta S(\tau)$. The corresponding initial conditions are

$$\begin{gathered} g_s(\xi,0) = 1, \quad g_o(\xi,0) = 1, \quad g_b(\xi,0) = 0, \quad \phi(\xi,0) = 0, \\ h(\xi,0) = H_0\left(1 - \xi^2\right), \quad S(0) = 1, \end{gathered} \tag{C.3}$$

and the boundary conditions are

$$
\begin{gathered}
\left.\frac{\partial h}{\partial \xi}\right|_{(0,\tau)} = 0, \quad \left.\frac{\partial \phi}{\partial \xi}\right|_{(0,\tau)} = 0, \\
\left.\frac{\partial g_s}{\partial \xi}\right|_{(0,\tau)} = 0, \quad \left.\frac{\partial g_o}{\partial \xi}\right|_{(1/\delta S,\tau)} = 0, \quad \left.\frac{\partial g_b}{\partial \xi}\right|_{(0,\tau)} = \left.\frac{\partial g_b}{\partial \xi}\right|_{(1,\tau)} = 0, \\
g_s(1,\tau) = g_o(1,\tau), \quad \left.\frac{\partial g_s}{\partial \xi}\right|_{(1,\tau)} = \left.\frac{\partial g_o}{\partial \xi}\right|_{(1,\tau)}, \\
u(0,\tau) = 0, \quad \left.\frac{\partial u}{\partial \xi}\right|_{(1,\tau)} = \frac{S(\tau)\Psi_n}{2}\phi(1,\tau)g_b(1,\tau).
\end{gathered}
\tag{C.4}
$$

To describe the numerical scheme, we use the notation $u_j^l = u(\xi_j, \tau_l)$ to represent the value of variables at grid points. We define the temporal grid $\tau_l = (l-1)\Delta\tau$, for $l = 1, \ldots, M$, such that M is the number of time steps, and $\Delta\tau = T/(M-1)$ is the constant time step size. We define the spatial grid for the colony biofilm to be $\xi_j = (j-1)\Delta\xi$ for $j = 1, \ldots, N$, where N is the number of grid points, and $\Delta\xi = 1/(N-1)$ is the constant grid spacing. In unoccupied regions of the substratum, we define $\xi_j^o = 1 + (j-1)\Delta\xi^o$, where the constant grid spacing $\Delta\xi^o = (1/\delta S - 1)/(N-1)$ is chosen such that $\xi_N^o = 1/\delta S$. Since the grid ξ^o depends on τ, we reinitialise it every time step after updating S. We use a Crank–Nicolson method to solve (C.2), similar to Tam [3] and Tam et al. [4]. We use an upwind spatial discretisation for the advection term in (C.2a), and central differences for spatial derivatives arising from applying the change of variables to derivatives with respect to t. At interior grid points, this leads to the scheme

$$\frac{h_j^{l+1}-h_j^l}{\Delta\tau}-\frac{\xi_j u_N^l}{S^l}\left(\frac{h_{j+1}^{l+1/2}-h_{j-1}^{l+1/2}}{2\Delta\xi}\right)+\frac{u_j^l h_j^{l+1/2}-u_{j-1}^l h_{j-1}^{l+1/2}}{S^l\Delta\xi}=\Psi_n\phi_j^l {g_b}_j^l h_j^{l+1/2}, \tag{C.5a}$$

$$\frac{\phi_j^{l+1}-\phi_j^l}{\Delta\tau}+\left(\frac{u_j^l-\xi_j u_N^l}{S^l}\right)\left(\frac{\phi_{j+1}^{l+1/2}-\phi_{j-1}^{l+1/2}}{2\Delta\xi}\right)=\phi_j^{l+1/2}\left[\Psi_n {g_b}_j^l\left(1-\phi_j^l\right)-\Psi_d\right], \tag{C.5b}$$

$$\begin{aligned}&\frac{{g_s}_j^{l+1}-{g_s}_j^l}{\Delta\tau}-\frac{\xi_j u_N^l}{S^l}\left(\frac{{g_s}_{j+1}^{l+1/2}-{g_s}_{j-1}^{l+1/2}}{2\Delta\xi}\right)\\ &=\frac{D}{{S^l}^2}\left(\frac{{g_s}_{j+1}^{l+1/2}-2{g_s}_j^{l+1/2}+{g_s}_{j-1}^{l+1/2}}{\Delta\xi^2}\right)-\delta Q^*\left({g_s}_j^{l+1/2}-{g_b}_j^l\right),\end{aligned} \tag{C.5c}$$

$$\frac{{g_o}_j^{l+1}-{g_o}_j^l}{\Delta\tau}-\frac{\xi_j^o u_N^l}{S^l}\left(\frac{{g_o}_{j+1}^{l+1/2}-{g_o}_{j-1}^{l+1/2}}{2\Delta\xi^o}\right)=\frac{D}{{S^l}^2}\left(\frac{{g_o}_{j+1}^{l+1/2}-2{g_o}_j^{l+1/2}+{g_o}_{j-1}^{l+1/2}}{{\Delta\xi^o}^2}\right), \tag{C.5d}$$

$$\begin{aligned}&h_j^{l+1}\left(\frac{{g_b}_j^{l+1}-{g_b}_j^l}{\Delta\tau}\right)-\frac{\xi_j u_N^l}{S^l}\left(\frac{{g_b}_{j+1}^{l+1/2}-{g_b}_{j-1}^{l+1/2}}{2\Delta\xi}\right)+\frac{u_{j+1}^l h_{j+1}^{l+1}{g_b}_{j+1}^{l+1/2}-u_{j-1}^l h_{j-1}^{l+1}{g_b}_{j-1}^{l+1/2}}{2\Delta\xi S^l}\\ &=\frac{\left(h_{j+1}^{l+1}+h_j^{l+1}\right)\left({g_b}_{j+1}^{l+1/2}-{g_b}_j^{l+1/2}\right)-\left(h_j^{l+1}+h_{j-1}^{l+1}\right)\left({g_b}_j^{l+1/2}-{g_b}_{j-1}^{l+1/2}\right)}{2{S^l}^2\Delta\xi^2}\\ &\quad+Q^*\left({g_s}_j^{l+1}-{g_b}_j^{l+1/2}\right)-\Upsilon\phi_j^{l+1}{g_b}_j^{l+1/2}h_j^{l+1},\end{aligned} \tag{C.5e}$$

$$\begin{aligned}&\frac{2}{{S^l}^2}\frac{\left(h_{j+1}^l+h_j^l\right)\left(u_{j+1}^l-u_j^l\right)-\left(h_j^l+h_{j-1}^l\right)\left(u_j^l-u_{j-1}^l\right)}{\Delta\xi^2}-\lambda^* u_j^l\\ &=\frac{\Psi_n}{S^l}\left(\frac{\phi_{j+1}^l {g_b}_{j+1}^l h_{j+1}^l-\phi_{j-1}^l {g_b}_{j-1}^l h_{j-1}^l}{\Delta\xi}\right),\end{aligned} \tag{C.5f}$$

$$\frac{S^{l+1}-S^l}{\Delta\tau}=\frac{u_N^{l+1/2}}{2}, \tag{C.5g}$$

for $j=2,\ldots,N-1$, and $l=1,\ldots M-1$. In (C.5), for compactness we write the scheme with some terms approximated halfway between time steps. In practice, we approximate these terms using centred averages, for example

$$u_j^{l+1/2}=\frac{u_j^{l+1}-u_j^l}{2}, \tag{C.6}$$

and so on for other variables. Since ξ^o depends on S, after updating S based on (C.5g) we interpolate linearly to update the nutrient concentrations g_s and g_o, to maintain compatibility with the updated colony biofilm domain.

It remains to specify the numerical schemes for the boundary conditions. By the same argument as Ward and King [11], since $h(S(0),0)=0$ the PDE (B.43a) guarantees that $h(S(t),t)=0$ for all t. Therefore, for convenience we impose $h_N = 0$ directly. To ensure continuity of the nutrient concentration in the substratum, we apply the Dirichlet conditions $g_s(1, \tau) = g_o(1, \tau) = a$. The correct value of a is such that $\partial_\xi g_s(1, \tau) = \partial_{\xi^o} g_o'(1, \tau)$, and we obtain this value numerically using the Newton–Raphson method, using g_s at $\xi = 1$ from the previous time step as the initial guess. Once we have found a, the numerical schemes for the boundary conditions read

$$\frac{-3h_1^l + 4h_2^l - h_3^l}{2\Delta\xi} = 0, \tag{C.7a}$$

$$h_N = 0, \tag{C.7b}$$

$$\frac{-3\phi_1^l + 4\phi_2^l - \phi_3^l}{2\Delta\xi} = 0, \tag{C.7c}$$

$$\frac{\phi_N^{l+1} - \phi_N^l}{\Delta\tau} = \phi_N^{l+1/2} \left[\Psi_n {g_b}_N^l \left(1 - \phi_N^l\right) - \Psi_d \right], \tag{C.7d}$$

$$\frac{{g_s}_1^{l+1} - {g_s}_1^l}{\Delta\tau} = \frac{2D}{{S^l}^2} \left(\frac{{g_s}_2^{l+1/2} - {g_s}_1^{l+1/2}}{\Delta\xi^2} \right) - \delta Q^* \left({g_s}_1^{l+1/2} - {g_b}_1^l \right), \tag{C.7e}$$

$${g_s}_N^{l+1} = a, \tag{C.7f}$$

$${g_o}_1^{l+1} = a, \tag{C.7g}$$

$$\frac{{g_o}_N^{l+1} - {g_o}_N^l}{\Delta\tau} = \frac{2D}{{S^l}^2} \left(\frac{{g_o}_{j-1}^{l+1/2} - {g_o}_j^{l+1/2}}{{\Delta\xi^o}^2} \right), \tag{C.7h}$$

$$\begin{gathered} h_1^{l+1} \left(\frac{{g_b}_1^{l+1} - {g_b}_1^l}{\Delta\tau} \right) + \frac{h_1^{l+1} {g_b}_1^{l+1}}{S^l} \left(\frac{-3u_1^l + 4u_2^l - u_3^l}{2\Delta\xi} \right) \\ = \frac{\left(h_2^{l+1} + h_1^{l+1}\right)\left({g_b}_2^{l+1/2} - {g_b}_1^{l+1/2}\right)}{{S^l}^2 \Delta\xi^2} + Q^* \left({g_s}_1^l - {g_b}_1^{l+1/2} \right) - \Upsilon \phi_1^{l+1} {g_b}_1^{l+1/2} h_1^{l+1}, \end{gathered} \tag{C.7i}$$

$${g_b}_N^{l+1} = Q^* {g_s}_N^{l+1} \left[Q^* + u_N^l \left(\frac{3h_N^{l+1} - 4h_{N-1}^{l+1} + h_{N-2}^{l+1}}{2\Delta\xi} \right) \right]^{-1}, \tag{C.7j}$$

$$u_1^l = 0, \tag{C.7k}$$

$$\frac{3u_N^l - 4u_{N-1}^l + u_{N-2}^l}{2\Delta\xi} = \frac{S^l \Psi_n}{2} \phi_N^l {g_b}_N^l. \tag{C.7l}$$

The expression (C.7j) arises by expanding the PDE (C.2e), applying $h = 0$ and $\partial_\xi g_b = 0$ at $\xi = 1$, and discretising the resulting expression. Together with the initial conditions (C.3), this completes the scheme for solving the full model (B.43)–(B.45) numerically.

C.1 Parameter Optimisation Tests

Repeated Parameter Estimation: Table C.1 presents parameter estimation results for five independent runs of the optimisation routine with the mean experimental data. These results confirm that the optimisation procedure converges to a very similar local minimum in $\rho(\theta^*, a)$ each run.

Table C.1: Optimal dimensionless parameters $\theta^*(a)$, expressed to four significant figures, for each agar density based on mean experimental data and 5 repetitions of the optimisation routine.

Run	a	Ψ_n	Ψ_d	Q^*	Υ	λ^*	$\rho(\theta^*, a)$
1	0.6	0.3030	0.007766	7.400	7.881	0.6733	0.04374
	0.8	0.3651	0.007471	6.539	7.336	1.042	0.05364
	1.2	0.4093	0.007551	4.481	6.462	1.848	0.06360
	2.0	0.3022	0.008347	3.270	5.007	2.670	0.06254
2	0.6	0.3009	0.007768	7.601	7.861	0.6693	0.04372
	0.8	0.3651	0.007473	6.533	7.332	1.042	0.05364
	1.2	0.4091	0.007552	4.480	6.459	1.847	0.06360
	2.0	0.3022	0.008346	3.271	5.009	2.670	0.06254
3	0.6	0.3011	0.007765	7.602	7.867	0.6696	0.04372
	0.8	0.3650	0.007471	6.551	7.335	1.041	0.05364
	1.2	0.4095	0.007551	4.474	6.463	1.849	0.06360
	2.0	0.3023	0.008344	3.275	5.015	2.671	0.06254
4	0.6	0.3013	0.007766	7.579	7.869	0.6700	0.04372
	0.8	0.3646	0.007472	6.561	7.330	1.041	0.05364
	1.2	0.4099	0.007548	4.479	6.475	1.850	0.06360
	2.0	0.3022	0.008347	3.272	5.008	2.670	0.06254
5	0.6	0.3009	0.007767	7.610	7.862	0.6692	0.04372
	0.8	0.3648	0.007473	6.550	7.330	1.041	0.05364
	1.2	0.4092	0.007553	4.477	6.457	1.848	0.06360
	2.0	0.3024	0.008344	3.273	5.014	2.672	0.06254

Numerical Grid Convergence: Since each evaluation of the objective function in the parameter estimation method requires solving the model numerically once, the parameter estimation procedure is computationally expensive. With $N_\xi = 401$ grid points and $N_\tau = 1601$ time steps, obtaining the optimal parameters for one set of experimental data took approximately 6.5 hours on an Intel Core i7-3770 CPU @ 3.40GHz × 4 running Linux Mint 22.2. Owing to the constraint of computational cost, we use a relatively coarse numerical grid to obtain the results.

These numerical solutions will contain numerical error, so we repeat the parameter estimation using different grid spacing and time step sizes, to ensure that our conclusions remain valid as the numerical grid is refined.

Table C.2: Parameter estimation results for different grid spacing and time step sizes, and 0.6% agar.

Parameter	N_τ N_ξ	101	201	401	801	1601
Ψ_n	25	0.3014	0.3033	0.3016	0.3019	0.3009
	51	0.3008	0.3029	0.3014	0.3023	0.3012
	101	0.3002	0.3023	0.3010	0.3018	0.3009
	201	0.2993	0.3018	0.3002	0.3008	0.3002
	401	0.2982	0.3009	0.2995	0.2998	0.2992
Ψ_d	25	0.007586	0.007662	0.007662	0.007695	0.007699
	51	0.007639	0.007721	0.007720	0.007754	0.007754
	101	0.007687	0.007768	0.007768	0.007802	0.007802
	201	0.007729	0.007811	0.007808	0.007843	0.007844
	401	0.007759	0.007844	0.007840	0.007875	0.007876
Q^*	25	11.31	10.20	10.08	9.942	9.961
	51	9.316	8.549	8.455	8.291	8.349
	101	8.292	7.617	7.591	7.462	7.498
	201	7.721	7.060	7.062	6.986	6.996
	401	7.413	6.757	6.744	6.692	6.704
Υ	25	8.745	8.780	8.747	8.759	8.733
	51	8.219	8.228	8.203	8.223	8.206
	101	7.890	7.882	7.862	7.879	7.867
	201	7.664	7.648	7.623	7.637	7.628
	401	7.504	7.490	7.470	7.479	7.467
λ^*	25	0.6958	0.7239	0.7300	0.7354	0.7352
	51	0.6608	0.6839	0.6900	0.6963	0.6960
	101	0.6424	0.6640	0.6694	0.6750	0.6752
	201	0.6305	0.6518	0.6569	0.6614	0.6623
	401	0.6223	0.6436	0.6492	0.6532	0.6539
$\rho(\theta^*, a)$	25	0.03920	0.03967	0.04041	0.04045	0.04040
	51	0.04136	0.04162	0.04234	0.04241	0.04236
	101	0.04230	0.04310	0.04372	0.04379	0.04375
	201	0.04413	0.04430	0.04485	0.04488	0.04483
	401	0.04487	0.04516	0.04573	0.04573	0.04565

Table C.3: Parameter estimation results for different grid spacing and time step sizes, and 2.0% agar.

Parameter	N_τ / N_ξ	101	201	401	801	1601
Ψ_n	25	0.3032	0.3059	0.3043	0.3054	0.3042
	51	0.3016	0.3042	0.3041	0.3048	0.3044
	101	0.3001	0.3023	0.3022	0.3031	0.3028
	201	0.2979	0.3002	0.2999	0.3005	0.3003
	401	0.2954	0.2979	0.2976	0.2983	0.2979
Ψ_d	25	0.008137	0.008201	0.008203	0.008230	0.008238
	51	0.008216	0.008281	0.008276	0.008309	0.008308
	101	0.008282	0.008352	0.008346	0.008378	0.008377
	201	0.008342	0.008411	0.008407	0.008437	0.008439
	401	0.008392	0.008460	0.008455	0.008486	0.008488
Q^*	25	4.950	4.635	4.626	4.573	4.580
	51	4.063	3.813	3.767	3.716	3.726
	101	3.525	3.299	3.273	3.225	3.228
	201	3.205	2.996	2.967	2.936	2.938
	401	3.028	2.810	2.789	2.760	2.768
Υ	25	6.287	6.240	6.213	6.228	6.201
	51	5.575	5.519	5.505	5.497	5.497
	101	5.102	5.015	5.010	5.001	5.000
	201	4.771	4.679	4.664	4.657	4.658
	401	4.548	4.446	4.436	4.429	4.432
λ^*	25	2.990	3.088	3.098	3.124	3.117
	51	2.724	2.801	2.824	2.842	2.843
	101	2.585	2.650	2.670	2.687	2.689
	201	2.495	2.556	2.574	2.587	2.590
	401	2.434	2.493	2.511	2.524	2.526
$\rho(\theta^*, a)$	25	0.05883	0.05908	0.05996	0.05978	0.05981
	51	0.06039	0.06058	0.06145	0.06128	0.06131
	101	0.06161	0.06170	0.06254	0.06237	0.06240
	201	0.06253	0.06266	0.06344	0.06327	0.06330
	401	0.06322	0.06336	0.06416	0.06397	0.06399

The convergence results in Tables C.2 and C.3 suggest that N_τ has no consistent effect on the estimated parameter values when $N_\tau > 201$. Consequently, we consider the results with $N_\tau = 1601$ to be approximately independent of time step size, $\Delta\tau$. However, the results may not be independent of $\Delta\xi$, because the parameter estimates in Tables C.2 and C.3 vary with N_ξ. Doubling the number of grid points and time steps yields small changes in Ψ_n, Ψ_d, and λ^*, and up to 10% variation in Q^* and Υ. These results align with the sensitivity analyses in the main manuscript, where Q^* was more difficult to identify, and Q^* and Υ tended to vary in concert with each other. The variation in optimal parameters could also be due to randomness inherent in the optimisation procedure, in addition to the grid spacing. As Tables C.2 and C.3 indicate, these variations do not affect the qualitative conclusions of the manuscript.

C.2 Heat Maps

See below of additional parameter pair heat maps indicating how model parameters influence $\rho(\theta, a)$, the distance between the model and experimental results. Figure C.1 shows that the parameter trends on hard agar are similar to the trends on soft agar.

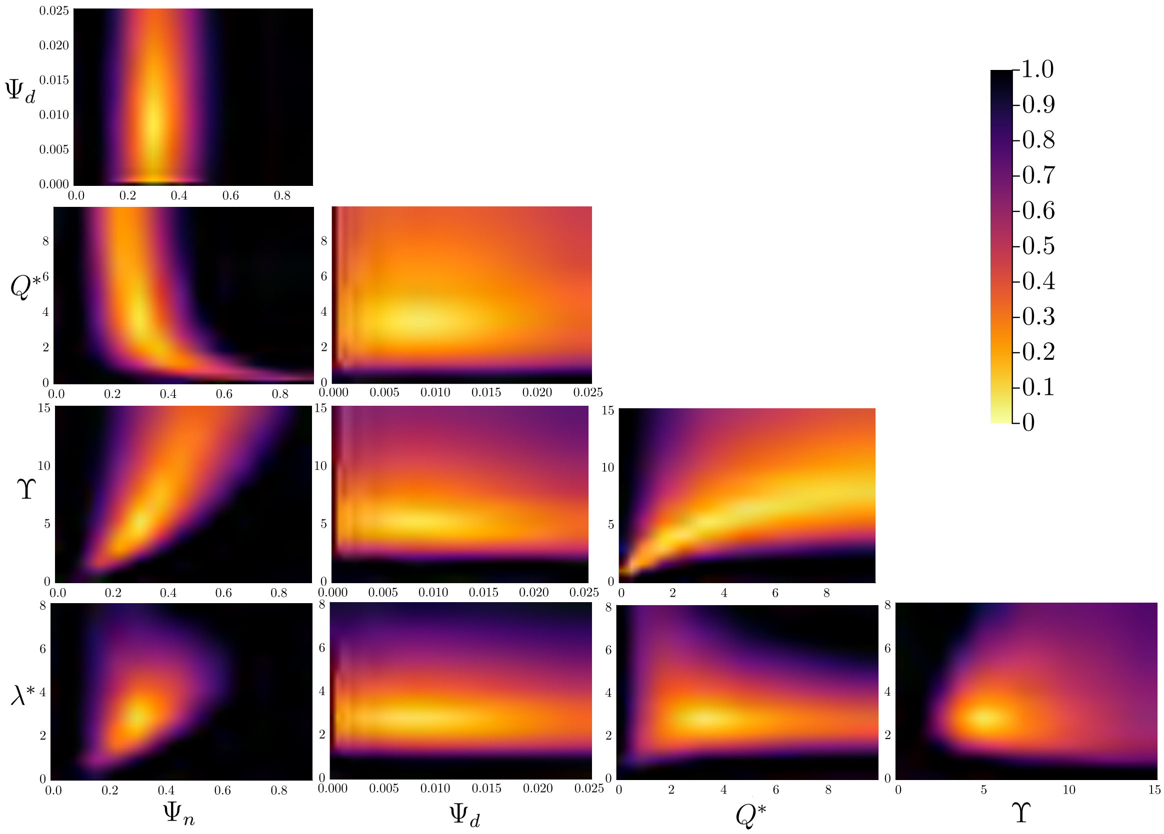

Figure C.1: Parameter pair heat maps for hard 2.0% agar. Plots represent the distance between the numerical solution and experimental data, $\rho(\theta, a)$, for given parameter combination. Unless otherwise stated, parameters take the optimal values. When varied, each parameter ranges from zero to three times the optimal value.

D Code and Data Availability

Experimental data, numerical code, and additional results for image processing and solving the thin-film model are available on GitHub.

References

[1] W. J. Middelhoven, B. Broekhuizen, and J. van Eijk, “Detection, with the Dye Phloxine B, of Yeast Mutants Unable to Utilize Nitrogenous Substances as the Sole Nitrogen Source”, *J. Bacteriol.* 128 (1976), pp. 851–852, DOI: 10.1128/jb.128.3.851-852.1976.

[2] J. F. Cannon, J. B. Gibbs, and K. Tatchell, “Supperssors of the Ras2 Mutation of *Saccharomyces Cerevisiae*”, *Genetics* 113 (1986), pp. 247–264, DOI: 10.1093/genetics/113.2.247.

[3] A. Tam, “Mathematical Modelling of Pattern Formation in Yeast Biofilms”, PhD thesis, The University of Adelaide, 2019, HDL: 2440/122613.

[4] A. Tam, J. E. F. Green, S. Balasuriya, E. L. Tek, J. M. Gardner, J. F. Sundstrom, V. Jiranek, and B. J. Binder, “A Thin-Film Extensional Flow Model for Biofilm Expansion by Sliding Motility”, *Proc. Royal Soc. A* 475 (2019), 20190175, DOI: 10.1098/rspa.2019.0175.

[5] A. K. Y. Tam, B. Harding, J. E. F. Green, S. Balasuriya, and B. J. Binder, “Thin-Film Lubrication Model for Biofilm Expansion under Strong Adhesion”, *Phys. Rev. E* 105 (2022), 014408, DOI: 10.1103/PhysRevE.105.014408.

[6] S. Srinivasan, C. N. Kaplan, and L. Mahadevan, “A Multiphase Theory for Spreading Microbial Swarms and Films”, *eLife* 8 (2019), e42697, DOI: 10.7554/eLife.42697.

[7] D. A. Drew, “Mathematical Modeling of Two-Phase Flow”, *Annu. Rev. Fluid Mech.* 15 (1983), pp. 261–291, DOI: 10.1146/annurev.fl.15.010183.001401.

[8] I. Klapper, C. J. Rupp, R. Cargo, B. Purvedorj, and P. Stoodley, “Viscoelastic Fluid Description of Bacterial Biofilm Material Properties”, *Biotechnol. Bioeng.* 80 (2002), pp. 289–296, DOI: 10.1002/bit.10376.

[9] S. J. Franks, H. M. Byrne, J. R. King, J. C. E. Underwood, and C. E. Lewis, “Modelling the Early Growth of Ductal Carcinoma in Situ of the Breast”, *J. Math. Biol.* 47 (2003), pp. 424–452, DOI: 10.1007/s00285-003-0214-x.

[10] R. D. O’Dea, S. L. Waters, and H. M. Byrne, “A Multiphase Model for Tissue Construct Growth in a Perfusion Bioreactor”, *Math. Med. Biol.* 27 (2010), pp. 95–127, DOI: 10.1093/imammb/dqp003.

[11] J. P. Ward and J. R. King, “Thin-Film Modelling of Biofilm Growth and Quorum Sensing”, *J. Eng. Math.* 73 (2012), pp. 71–92, DOI: 10.1007/s10665-011-9490-4.

[12] G. Lemon, J. R. King, H. M. Byrne, O. E. Jensen, and K. M. Shakesheff, “Mathematical Modelling of Engineered Tissue Growth Using a Multiphase Porous Flow Mixture Theory”, *J. Math. Biol.* 52 (2006), pp. 571–594, DOI: 10.1007/s00285-005-0363-1.

[13] D. A. Drew and L. A. Segel, “Averaged Equations for Two-Phase Flows”, *Stud. Appl. Math.* 50 (1971), pp. 205–231, DOI: 10.1002/sapm1971503205.

[14] G. Forgacs, R. A. Foty, Y. Shafrir, and M. S. Steinberg, “Viscoelastic Properties of Living Embryonic Tissues: A Quantitative Study”, *Biophys. J.* 74 (1998), pp. 2227–2234, DOI: 10.1016/S0006-3495(98)77932-9.

[15] R. M. Harshey, “Bacterial Motility on a Surface: Many Ways to a Common Goal”, *Annu. Rev. Microbiol.* 57 (2003), pp. 249–273, DOI: 10.1146/annurev.micro.57.030502.091014.

[16] J. Recht, A. Martínez, S. Torello, and R. Kolter, “Genetic Analysis of Sliding Motility in *Mycobacterium smegmatis*”, *J. Bacteriol.* 182 (2000), pp. 4348–4351, DOI: 10.1128/JB.182.15.4348-4351.2000.

[17] R. D. O’Dea, S. L. Waters, and H. M. Byrne, “A Two-Fluid Model for Tissue Growth within a Dynamic Flow Environment”, *Eur. J. Appl. Math.* 19 (2008), pp. 607–634, DOI: 10.1017/S0956792508007687.

[18] S. J. Franks and J. R. King, “Interactions between a Uniformly Proliferating Tumour and Its Surroundings: Uniform Material Properties”, *Math. Med. Biol.* 20 (2003), pp. 47–89, DOI: 10.1093/imammb/20.1.47.

[19] S. R. Lubkin and T. L. Jackson, “Multiphase Mechanics of Capsule Formation in Tumors”, *J. Biomech. Eng.* 124 (2002), pp. 237–243, DOI: 10.1115/1.1427925.

[20] A. Tam, J. E. F. Green, S. Balasuriya, E. L. Tek, J. M. Gardner, J. F. Sundstrom, V. Jiranek, and B. J. Binder, “Nutrient-Limited Growth with Non-Linear Cell Diffusion as a Mechanism for Floral Pattern Formation in Yeast Biofilms”, *J. Theor. Biol.* 448 (2018), pp. 122–141, DOI: 10.1016/j.jtbi.2018.04.004.